UNIVERSITAT POLITÈCNICA DE CATALUNYA
BARCELONATECH

MASTER THESIS

Mission Analysis for a Swarm of Femtosatellites to Study the Lower Thermosphere

Nurmakhan Aidynbay

SUPERVISED BY

Jordi Gutiérrez Cabello

Universitat Politècnica de Catalunya
Master in Aerospace Science & Technology
February 2020

This Page Intentionally Left Blank

Mission Analysis for a Swarm of Femtosatellites to Study the Lower Thermosphere

BY

Nurmakhan Aidynbay

DIPLOMA THESIS FOR DEGREE

Master in Aerospace Science and Technology

AT

Universitat Politècnica de Catalunya

SUPERVISED BY:

Jordi Gutiérrez Cabello

Department of Physics

This Page Intentionally Left Blank

ABSTRACT

The lower thermosphere (between 100 and 250 km) is badly known due to the scarcity of operating satellites in this region. Nevertheless, it is very relevant for the study of Earth-Sun relations, satellite re-entry forecasting, and climate change, among other disciplines.

We propose the analysis of a swarm of femtosatellites to directly analyze the thermosphere by means of a MEMS accelerometer onboard each satellite. The goal is to use the deceleration caused by drag to determine the local density, thus drawing a map of the thermosphere on multiple locations.

The shape of the satellites will be spherical (with a diameter of 5 or 10 cm), thus simplifying the measurement of drag. The mass distribution will be that of a spherical top (then, no attitude control), or will have the center of mass separated from the geometric center (thus providing aerodynamic stability).

Each satellite will also count with a MEMS GNSS receiver that will provide precise location and time-tagging to the measurements. A small onboard computer, mass storage system, radio transmitter, and primary battery will form the bus of the satellite.

The goal of this Master Thesis is to develop a self-consistent mission analysis of the mission, with special interest in comparing the properties of the non-stabilized and aerodynamically stabilized satellites.

The main objectives must be:

- Design and analysis of the optimal orbit for these satellites. Of particular interest is the study of the different alternatives for orbital injection and dissemination.
- Analysis of orbital decay using DRAMA. Evaluation of the risk for third-party satellites posed by a large swarm. Proposals for decreasing this risk.
- Data gathering strategy.
- Sources of noise for the accelerometer, both instrumental and environmental.
- Communication strategy. Determination of the link budget, proposal for ground station typology and location.
- Energy budget. Analysis of mission's life limitations due to the endurance of the battery.
- Alternative scenarios for mission success. Identify and evaluate scenarios in which the mission cannot be accomplished in the planned way. For example, analyze possible mission procedures should the accelerometer fail.

This project is undertaken in collaboration with Prof. Igor Belokonov, Inter-University Department of Space Research, Samara University (Russia).

This Page Intentionally Left Blank

ACKNOWLEDGEMENTS

I would like to express my appreciation and gratitude to professor Jordi for his guidance, assistance and suggestions throughout this project development from it's beginning to the end.

I am sincerely thankful to my parents, sisters and brother for their unconditional support and help, encouragement and kindness throughout writing this thesis and in general to realize my dream of obtaining Master's degree.

I would like to mention all my friends for helping me not to give up and stand all stresses these years, especially my friends of this program with whom I spent most of studying time and staying in Castelldefels.

This Page Intentionally Left Blank

Table of Contents

List of Figures

List of tables

This Page Intentionally Left Blank

INTRODUCTION.

The next future space missions will require accurate prediction of the space vehicle trajectory, precise determination of its orbit, collision avoidance calculations with orbiting elements or debris, and reentry position determination of the space vehicle. The empirical models of atmosphere density have been widely used to effectively improve space mission development in such applications. The present empirical models of air density are based on observation data obtained from missions such as Drag and Atmospheric Neutral Density Explorer, SpinSat or QB50 among many others. In addition to this, the data of nongravitational accelerations and accurate position in orbit measured by onboard accelerometers and global navigation satellite system (GNSS) receivers has updated these models from missions such as the Gravity Recovery And Climate Experiment (GRACE) and Challenging Minisatellite Payload. The typical method used in mentioned missions to determine and correct the density of the atmosphere is to analyze measurements from mass spectrometers, accelerometers, GNSS receivers from Earth orbiting missions and satellite laser ranging from the ground. The mass spectrometer data describes the gas particle configuration around the spacecraft, whereas accelerometers data used to estimate satellite's non gravitational perturbations caused by the atmospheric drag. Also, the use of orbital data, often presented in the formof so-called two-line elements (TLE), or obtained by means of the GNSS receiver are crucial to estimate and update atmospheric density. Although TLE data resolution isn't high, it represents the average density for a certain time frame (Zhao, 2019).

The atmospheric density decrease depends exponentially with the orbit altitude and also depends on solar and geomagnetic activities, which lead to uncertainty rates of 10-30% or higher in current air density models. These variations and its causes in thermosphere at 100-300 km height have not been deeply studied due to lack of operational satellites in this region. The thermosphere is the layer of the atmosphere from 85 km up to 800 km above the ground where the solar extreme ultraviolet and soft X-rays are absorbed and exothermic reactions creates ions in the ionosphere. Thus, in order to improve our knowledge of Sun-Earth physics and missions' orbit computations, the lower thermospheric density must studied in depth to allow an update of current empirical air density models in this region. (Wakker, 2015).

The expansion of the electronic devices miniaturization paradigm to the space industry has boosted the opportunity to access space for universities and small research groups (even amateurs). As a perfect example of this trend, CubeSat missions can be considered where students participate and develop these missions under academic supervision. Startup, even firmly stablished, companies have found a new market to offer commercial-of-the-shelf products, modules and devices ready to use. This trend of decreasing mass, size and cost of satellite design created new categories of satellites such as mini-, micro-, nano-, pico- and femtosatellites as well as decreased the required time for mission and launch development. Table 0.1 summarizes the typical small satellite mass classification.

Table 0.1 Small mass classification.

Classification	Mass range, (kg)
Minisatellites	100-1000
Microsatellites	10-100
Nanosatellites	1-10
Picosatellites	0.1-1
Femtosatellites	less than 0.1

In this Master's thesis, we perform a preliminary mission analysis of a swarm of femtosatellites for direct measurements in the lower thermosphere. The main idea is to use the deceleration caused by the atmospheric drag to determine the local atmospheric density. These direct, in situ measurement will be taken over by three single axis onboard accelerometers which are assembled together inside a spherical structure that simplifies drag measurement (as attitude is unimportant, and the drag coefficient simplifies). Moreover, each satellite will be equipped with a GNSS receiver onboard to provide precise position in orbit and time tagging to the measurements. Also, it is important to mention its other subsystems such as onboard microcomputer, flash memory for data storage, transmitter and primary battery that will form the femtosatellite bus.

The project structural organization breaks down into chapters as follows. Chapter one provides an overview of the Earth space environment, the effects of solar activity, the atmospheric layers and the aim of lower thermosphere studies. Then in Chapter two we provide the overview of the mission, the set of primary requirements and the main features of the femtosatellite payload and structure to meet these requirements. Next, Chapter three will deal with the analysis and selection of the orbits and the launching opportunities. Moreover, there will be a discussion of the results from orbit simulations based on variations of the proposed femtosatellite configuration such as different mass, radius and drag coefficient; this simulation is performed with ESA's Debris Assessment and Mitigation Analysis (DRAMA) tool. Afterwards, Chapter four will present the mission data gathering strategy, the link budget, as well as power and mass budgets based on suggested femtosatellite design from previous chapter. In the last chapter the use of accelerometers data, in orbit position data obtained by GNSS receiver and TLE data for thermospheric density determination will be explained in detail. Finally, in the conclusion part, the results of the project development and required improvements in future work will be briefly summarized.

Chapter 1

THE SPACE ENVIRONMENT.

This chapter describes the effects that spacecrafts and rockets usually experience during launch and operation in space. The Earth surrounding space can be defined as a hazardous vacuum environment where spacecrafts are affected by high energy particles and highly reactive species, electromagnetic radiation, flows of dense plasma and variable densities of neutral gases at low Earth orbit (LEO). The solar activity effects, basic structure of the atmosphere and the purpose of the proposed thermosphere study will be presented in following sections.

1.1. The Earth's Environment.

There is no fixed upper boundary for Earth's atmosphere, as it simply decreases in density (as well as changes in composition and thermodynamic properties) and it can be detected up to one Earth radius above the surface. The atmosphere causes a drag force that affect spacecraft during launch and re-entry. Consequently, the drag is correlated to the density of the atmosphere and, to a lesser extent, to its particle composition which depend on altitude as well as solar and geomagnetic activity. Moreover, the neutral gas atmosphere above 100 km is ionized by solar extreme ultraviolet (EUV) and soft X rays radiation creating the ionosphere; its influence on radio signals propagation is the main effect on design of spacecraft apart of chemical and charging effects. It can be said that ionosphere ends at 1000 km but, again, there is no fixed upper boundary. This is an environment of low-density and high-energy charged particles, whose upper reaches intersect with Van Allen radiation belts. The magnetosphere itself is considered as part of the magnetic shielding from the solar wind emitted by the Sun at speeds ranging from 300 to 800 km/s. Figure 1.1 illustrates a schematic structure of Sun-Earth interactions.

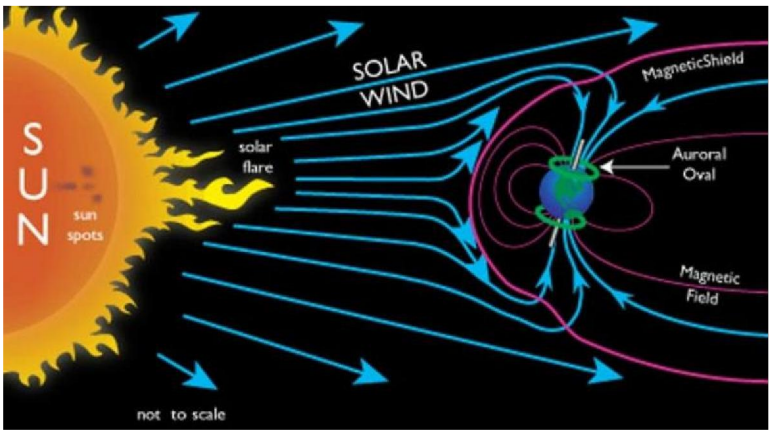

Figure 1.1 Influence of the Sun on the Earth. (Heller, 2018)

The near Earth's space environment is affected by the magnetic activity on the Sun (mainly originated in sunspots and protuberances) via some natural processes. The main source of energy for the thermosphere is the solar EUV and X-ray radiations, which is highly variable with time, and so their intensity is strongly correlated to 11-year solar activity cycle that can be seen in figure 1.2. Hence, the solar cycles (with its changes in sunspot activity and frequency of protuberances and other energetic solar phenomena) leads to the variations in the density of Earth's high atmosphere. Solar flares, high energy explosions occurring in active regions produce copious fluxes of EUV and X-ray radiation that cause disturbances in the atmosphere and ionosphere. The blasts of magnetised plasma clouds in coronal mass ejections (CMEs) from active regions, emitted with very high speeds, are the source for shock waves in solar wind. These waves are powerful particle accelerators which generate solar energetic particles (SEPs) which reach the Earth now and then. In these cases, the shock wave and CME magnetic cloud can generate geomagnetic storms. The consequences of these storms are intense heating of the atmosphere above 100 km, turbulence, changes in ionosphere density and not permanent dynamic magnetosphere reconfigurations which leads to charged particles acceleration and Van Allen radiation belts' repopulation or intensification.

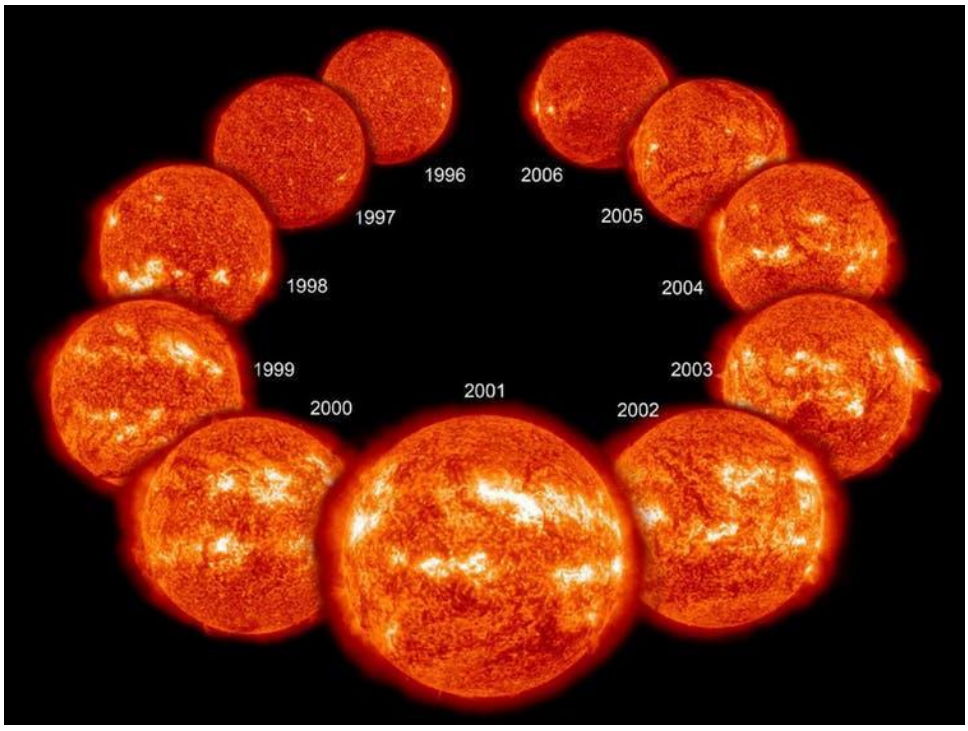

Figure 1.2 Images of the Sun during solar cycle 23 obtained by the SOHO satellite. Maximum solar activity happened in 2001. (Fraknoi, 2016).

The most aggressive among all solar activity consequences is particle radiation which consists of energetic (from about 10 keV to hundreds of MeV) electrons, protons, and ions (accelerated in solar flares and later trapped in the terrestrial magnetic field). Radiation is hazardous to human as well as to spacecraft and its electronic parts, which

are degraded or can even be destroyed. This is the main cause that limits space electronic systems lifetime (Pisacane, 2012).

1.2. The atmospheric layers.

The Earth's atmosphere is composed by the neutral gases layer that surrounds our planet. These gases profiles of density and pressure as a function of height are driven by physical phenomena of great complexity, and result in a temperature profile which helps to distinguish different atmospheric layers. Although the atmosphere structure is well determined, as illustrated in Figure 1.3, a brief explanation of each layer is beyond the scope of this work.

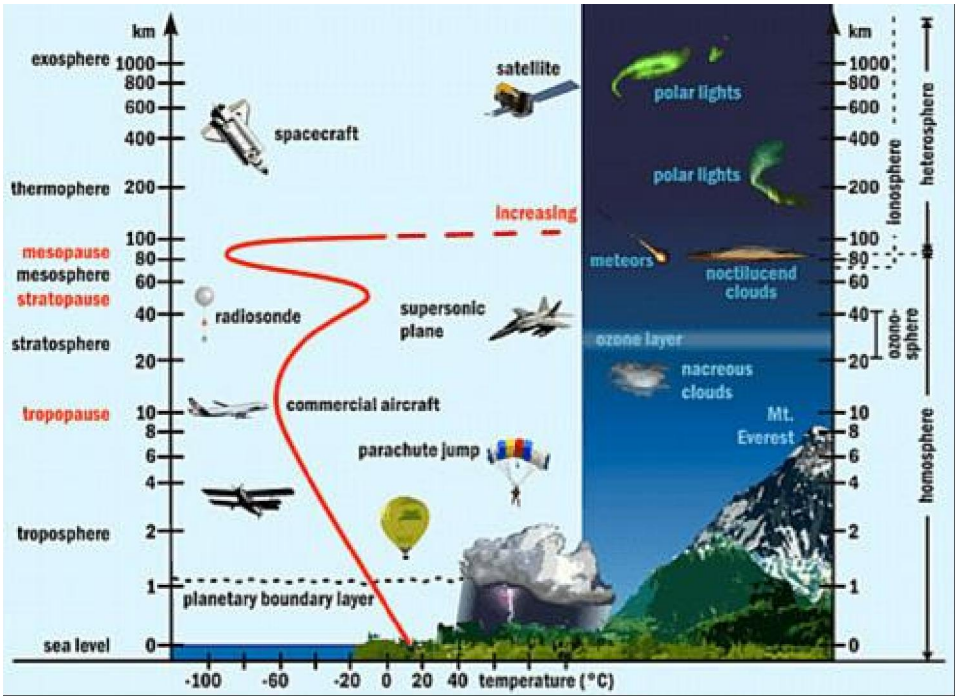

Figure 1.3 Vertical structure of the atmosphere (CivilsPro, 2018).

Earth's atmosphere, as already stated, is of great complexity and experiences dynamic changes in short timescales. Thus, its detailed description is far beyond the scope of the present study. It will serve us to state that the well mixed layer, called turbosphere, is limited to heights below approximately 80 – 100 km (depending on the state of the atmosphere). Over this altitude, chemical composition is also height-dependent.

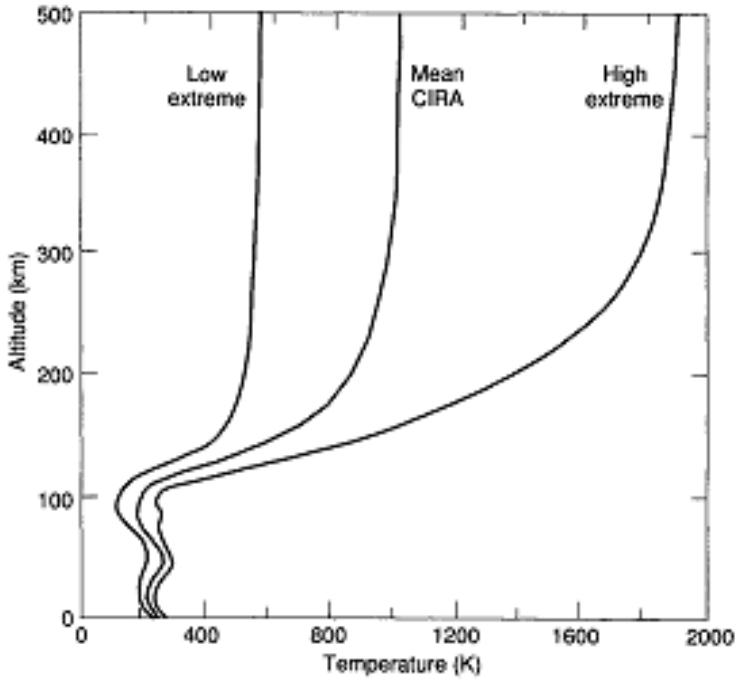

Figure 1.4 Temperature fluctuations during different solar activities.

The layer of interest for this study is the thermosphere, which extends from about 80 – 85 km to 600 – 800 km, again the limits depending on solar and geomagnetic activity.

In this region the temperature is very high and increases with altitude, as can be seen in Figure 1.4, due to exothermic reactions and absorption of solar EUV and X-rays. Most molecules are dissociated, in particular triatomic species like ozone or carbon dioxide, that are responsible for a great deal of IR re-emission of energy towards space. In this situation, the temperature can increase up to 1500 K, but usually it is in the range between 800 and 1200 K. It is important to note that the low atmospheric density ensures that thermal transport from atmospheric gases to solid objects (like satellites) is almost negligible, and thus this very hot part of the atmosphere does not contribute to heating of satellites. EUV solar radiation is also responsible for the ionization of part of the gas, giving rise to a neutral plasma that forms the ionosphere.

Thus, the ion to neutral thermal energy transfer, annual cycles and day - night heating cycles are dominated by changes of solar flux, which leads the thermosphere to be expanded and compressed hence leading to density variations. Moreover, plasma waves from the Sun causes Joule heating in the thermosphere, and high-energy charged particles precipitate along magnetic field lines of the Earth and affect the mass density breakdown of the thermosphere. These are very dynamic effects, being its characteristic evolution times measured in a few tens of minutes.

In the region higher than about 150 km the value of neutral density is very low; Physically, this means that atmospheric constituents' atoms or molecules do not collide between themselves; then, they move in ballistic trajectories in what we call a Free Molecular Flow. This will have an important impact in the determination of the drag coefficient, as gas-surface interactions become very complex.

At the altitude above 800 km, the last layer, the exosphere, begins and extends into space. Due to its extremely low density, again the motion of the particles is considered as ballistic trajectories and complete decoupling of gases takes place.

1.3. Interests of lower thermosphere studies.

The thermosphere at altitudes between 100 and 350 km has not been explored as thoroughly as other layers of atmosphere. The reason is simple to understand: it is beyond the maximum altitude of scientific balloons, whose record altitude is a bit less than 60 km, and is too low for achieving a stable orbit without the use of electric propulsion. First measurements were obtained from missions with highly elliptical orbits, but with this strategy only a few points of the thermosphere were probed in each passage, and the effect was so small that only the accumulated (and then averaged) effect could be measured. These days this in situ measurements is provided by probes like POPACS and still with shorter observation times than required for a thorough characterisation of the thermosphere. Satellite's high-performance remote sensing instruments for Earth Observation, operating from altitudes between 600 and 800 km, are not fully capable to fulfil in situ measurements of the thermosphere due to the weak signal absorption through the rarefied gas that composes it. Also, the same issue plagues ground lidar/radar remote sensing observations. These obstacles to obtaining remote measurements provides the justification of why there is not goof correlation between current models of atmospheric density in this layer. Some models are built with in situ measurements during short times while others are based on theoretical hypothesis related to the temperature of the exosphere.

In the late 1950s, the perturbations of satellite's orbits were investigated and this led to the first empirical air density modeling starting in the late 1960s. The Jacchia model was the first model developed at the Smithsonian Astrophysical Observatory in the US. Afterwards, Jacchia 71 was approved in 1972 as part of the International Reference Atmosphere (also known as CIRA-72) by the Committee on Space Research. This model has been updated over the decades and its last version is found in Jacchia and Bowman 2006 and 2008.

In 1978 another air density model, the so-called the Drag Temperature Model (DTM), was developed by the Groupe de Recherche de Géodésie Spatiale in France. The first DTM models were based on temperatures of neutral atmosphere and satellite drag observations. Based on high-quality data gathered by the mass spectrometer and accelerometer of the *Castor* satellite, a new, significantly updated model (DTM-94) was obtained. Next major modification, included in DTM-2009, made use of data obtained from *GRACE* and *CHAMP* missions. These models' issue is that the perturbations of data from onboard accelerometers only give information of the combination of parameters $C_D S\rho$. Air density modeling thus required assumptions on the C_D and S of each satellite; for altitudes less than 400 km it was assumed that C_D = 2.2, whereas for higher altitudes C_D steadily rises and at 800 km it reaches 2.6 value. The cross section S was estimated using attitude data from the satellites.

The MSIS model was developed by NASA Goddard Space Flight Center in the 1970s, and is based on observations of ground scatter radar and data of satellites' mass spectrometers. These models provide density and temperature of air elements not

related to C_D and S values, and so it beneficial in comparison to drag-derived density models. As a result, for CIRA-86 the MSIS-86 model is implemented. In the late 1990s the MSIS class models were further developed by the Naval Research Laboratory and the modified NRLMSISE00 was presented in 2002. This model includes not only the Jacchia and DTM orbit decay databases and the data of satellite accelerometer, but additionally data from incoherent scatter radar and mass spectrometer. Thus, CIRA-2012 updated model is considered as state-of-the-art model that combines all empirical models whose data are based on direct measurements obtained in the 1980s, 1990s and mid 2000s by several satellite sensors and ground equipment.

Therefore, the launch and operation of a femtosatellite swarm in this region would offer improved continuous in situ measurements. This mission would allow to broaden and update knowledge about the atmospheric density and dynamic changes within this layer. Then, data from this mission would be beneficial for all models of atmospheric density (Fernandez, 2011).

The application of density models of the thermosphere takes place in many fields of scientific research and studies, as well as in mission orbit computations which include prediction of the re-entry, design of required manoeuvres, and accurate orbit determination. Comparing and implementing of obtained data on thermosphere density from satellites operating in this region with present models could also improve our understanding of the Sun-Earth Physics. In addition, it would improve the trajectory determination of Earth observation missions to meet its scientific goals, other aspects of the mission analysis and operations, analysis of satellites orbiting lifetime, re-entry operations and planning of manoeuvres to avoid collisions. For a much thorough discussion of these applications, the interested reader can consult Doornbos (2011).

Chapter 2

PRELIMINARY SATELLITES LAYOUTS.

The mission overview, requirements list and the overview of the general design to meet these requirements will be described in this chapter. The following sections present theoretical air density determination, the set of mission requirements, and finally the main features of the femtosatellite payload and structure configuration both of the UPC and Samara designs.

2.1. Mission overview and its requirements.

The scientific aim of the mission is the direct measurement of the thermosphere density at heights up to 250–300 km above sea level. The femtosatellites swarm will be deployed on different polar orbit planes for full coverage of the thermosphere. The acceleration experienced by the femtosatellite due to the drag will be used as the primary method for thermosphere density determination, as shown in equation

$$D = \frac{1}{2}\rho V^2 S C_D = ma \quad \textbf{(2.1)}$$

Being spherical, the cross section is simply found via its satellite's radius of 5 cm and does not depend on its attitude. The values of velocity with regard to the atmosphere and the drag coefficient can be calculated by means of theoretical models, that are affected by some physical uncertainties. Thus, the orbital velocity at 300 km above ground is 7.8 km/s (for the International Space Station is 7.66 km/s), the drag coefficient for spherical object will be around 2 and, finally, the air mass density according to NRLMSISE-00 model is about 7.35×10^{-15} g/cm^3. As a result, from all available data the acceleration is found as

$$a = \frac{1}{2}\frac{SC_D}{m}\rho V^2 \quad \textbf{(2.2)}$$

which is about 3.5×10^{-6} m/s^2. This roughly derived value is the main constraint for the accuracy requirement of acceleration measurements.

According to the scientific aim of the mission, several requirements can be highlighted for every femtosatellite as well as for the complete swarm. Apart of the requirements for the satellite design itself, some others are related to their launch, orbital deployment and operation. Hence, the following list is determined as the primary requirements to fulfil the aim of the femtosatellites mission.

- the femtosatellites will be spherical, with a maximum mass of 100 grams, a diagonal inertia tensor with identical inertia moments and the centre of mass located in the sphere's geometrical centre.
- very small acceleration measurements (maximum accuracy of 10^{-6} m/s^2) must be performed once per second.
- precise measurements of the femtosatellites' location and time.
- seven days orbital operation lifetime.
- gathered data must be transmitted down to the ground.
- launch, deployment and operation environment loads endurance.
- orbit collision avoidance.

2.2. UPC design.

Based on previous studies, each individual femtosatellite will use commercial-of-the-shelf (COTS) micro-electro-mechanical systems (MEMS) technology. These components allow to meet requirements of the mission in terms of small size and mass, low rates of energy consumption, and low cost. We have chosen a spherical configuration with a radius up to 10 cm and mass up to 100 g. The payload is composed by: three single axis accelerometers mounted at right angles to measure the acceleration experienced by the satellite; a GNSS receiver to precisely fix time and position of measured accelerations; a flash memory to keep all obtained data; an on-board microcomputer to process and package all data; a transmitter to send all data down to certain ground stations; and a primary battery to provide required power to all these systems. Additionally, these set of systems will be fitted inside a spherical aerogel structure covered with a thin space-qualified plastic for passive thermal control.

2.2.1. Accelerometers.

These three single axis accelerometers must be identified as the critical part of the femtosatellite payload, for its acceleration measurements in the thermosphere will produce the most valuable data. Hence, it allows to fulfil mission primary objective, that is the determination of the air density at given height. These accelerometers are mounted in such a way that each one is oriented along one of the three axes (x, y, z). Thus, the total acceleration is the modulus of the vector formed with each axis acceleration determination. The main advantage of using three separate single-axis accelerometers instead of 3-axis accelerometers is that, in the latter case, one of the axes has a reduced accuracy in one direction.

As a result of searching COTS accelerometers based on MEMS, we have identified a device family from Silicon Designs Inc (SDI) that is close to fulfiling our requirements. These SDI single axis MEMS Variable Capacitive Accelerometers are of plug-and-play type. All 5 models from SDI stand out reliable performance, long term stability and low noise in a wide range of industrial and commercial applications. Figure 2.1 illustrates these accelerometers.

Figure 2.1 Low-cost and High-performance SDI modules (Silicon Designs, Inc, 2015).

Every SDI module represents a hermetically isolated SDI accelerometer chip with low noise inside a case of anodised aluminium. A regulation of voltage on-board and a reference of internal voltage completely remove the need for precision power supplies. The metal case is epoxy isolated and can be simply mounted with adhesive, two screws or magnetically attached. For our purposes, the casing is irrelevant and should be removed.

Among these modules our choice will be the high-performance SDI 2276 accelerometer module due to its large operational temperature range. This module can be distinguished from others with patented and improved SDI accelerometer chips that passed all necessary calibration and verification tests to ensure the maximum accuracy. Its key performance parameters are high sensitivity of 2000 mV/g and low noise rate of 10 μg $Hz^{-1/2}$ for ±2 g acceleration range and 2000 g mechanical shock, regarding to its electrical parameters its operation voltage rates are flexible between 8 and 32 VDC and its operation current is 10.5 mA. It is also important to say that its operation temperature range from –55 to +125 ºC, as well as its mass of just 9 grams for each module when the aluminum case mass included. As noted before, in order to minimize the overall mass of the three accelerometers the assembly metallic case should be removed. Moreover, this module is robust with long term stability. Figure 2.2 shows the schematic view of this module (sense element within case) while in tables its performance parameters are listed. All additional data related to this accelerometer can be found in reference (Silicon Design Inc, 2015) and in Annex A.

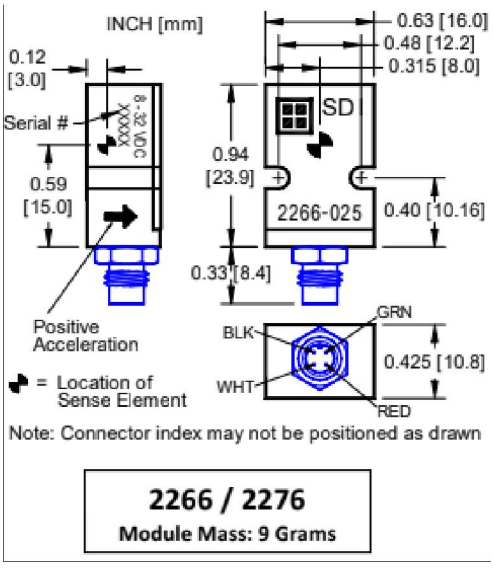

Figure 2.2 The schematic view of the selected SDI module (Silicon Designs, Inc, 2015)

2.2.2. GNSS receiver.

For precise time and position fixing during in situ measurements procedures, each femtosatellite will be equipped with a COCOM-free GNSS microchip receiver. COCOM (Coordinating Committee for Multilateral Export Controls) is a set of regulations enforced by the United States that restricts the usage of most commercial GNSS receivers to low altitudes (less than 18 km) and velocities (less than Ma = 1). The purpose, obviously, is difficulting the use of GPS receivers for missile guidance purposes.

The choice of this module will be based on previous studies and is the GNSS receiver from Warpspace. It is based on the Venus 838FLPx chip, and is able to use several constellations (GPS, GLONASS, Beidou, and EGNOS). Its mass is just 3 grams and the power consumption is 148.5 mW, which is a considerable load for the batteries. It provides a position accuracy of 2.5 m while the time accuracy is about 10^{-8} seconds; in both cases, the device perfectly fulfills our requirements.

The electric requirements are 3.3 V and 45 mA. It is not very rad-hard, withstanding just 5 krad, that is equivalent to a stay in low Earth orbit of one or two months (depending on the activity state of the Sun), but as our mission will last just one week, this gives us ample margin in this respect.

Figure 2.3 Warpspace GNSS receiver (WarpSpace).

2.2.3. Microcontroller.

The purpose of the microcomputer on board is to process and maintain all data obtained from other sensors and modules, to pack and to transmit them down to ground stations, as well as to monitor sensors and modules correct performance during mission operation. Additionally, it should determine the nearest ground stations via processing onboard GNSS data and ground stations positions for effective data transmission. Hence, the Microchip's microprocessor is of the utmost importance. The system selected is PIC18F1XK22, a model of 20 pins, 8 bit, and high performance with a relatively small size of 6×6×0.95 mm and low mass of 3 g.

Figure 2.4 Microchip PIC18F1XK22 (Microchip Technology, 2016).

Its electrical parameters must be also highlighted, with operation voltage rates of 2.3-5.5 V and nominal current of 25 mA. It has a wide operation temperature range with minimum temperature limit of –40ºC and maximum limit of +125 ºC. It utilizes three types of memory that are 16 Kbytes program memory, 512 bytes Random Access Memory (RAM) and 256 bytes Electrically Erasable Programmable Read Only Memory (EEPROM). This small memory sizes requires that gathered data are immediately written in the mass-storage device. The detailed parameters of the microprocessor can be seen in the product analysis paper from the provider (Microchip Technology) and can be found in Annex A. This device has an Analog to Digital Converter (ADC) with 10-bit resolution and 12 channels, but the data from GNSS receiver and accelerometers will be in digital format and so this feature will be unimportant. In terms of power consumption, its modes of power management provides very low energy consuming for Run mode, Idle mode and Sleep mode.

2.2.4. Flash memory.

The main purpose of flash memory onboard is to store all data processed by microprocessor and generated by sensors and modules before data transmission to the ground station. After detailed search, the devices from Micron company were found to be suitable with its wide range of available flash memory models with memory capacity from 8 Mb up to 2 Gb, a wide operation temperature that rates from –40 to +125 ºC, and different operational voltages and currents.

Hence, our choice would be the M25P64 Serial Flash Memory model which is 64 Mbit, about 1 g of mass with 8×8 mm in dimensions. Moreover, it provides an advanced mechanism of write protection. The memory organization is 128 sectors, each one consisting of 256 pages, each page 256 bites wide. Additionally, its Fast Program/Erase mode is used to speed up programming/erasing. Its operational minimum and maximum voltages are 2.7 and 3.6 V, operating and program currents are 8 and 15 mA, and operational minimum and maximum temperatures are –40 and +85 ºC, respectively.

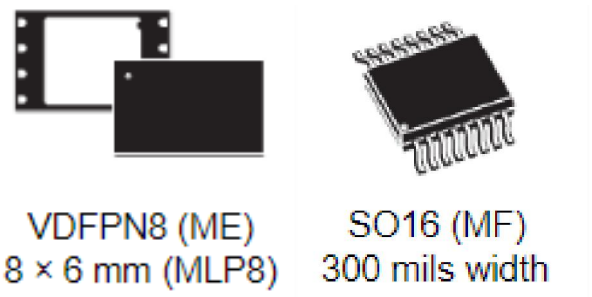

Figure 2.5 Micron's VDFPN8 Flash memory module (Micron).

Also, due to its different power modes (Active and Standby Power modes), this module has fairly low power consumption. When all internal cycles such as Program, Erase, Write, Status, or Register have finished, it switches to Standby Power mode and power consumption significantly drops. The external aspect of this device can be seen in Figure 2.5, and its full detailed specification is provided in the data sheet in Annex A.

2.2.5. Transmitter.

The aim of onboard transmitter is to downlink all the femtosatellite obtained and processed data to a set of suitable ground stations. To fulfill the mission, the transmitter offered by Silicon Labs Si4x55-C model is considered as a very suitable choice due to its operational features. This is a plug and play device which covers all major bands and its 20 pin QFN small size package of 3×3 mm and mass of just about 2 g makes this module space, mass and cost effective. It is an easy to use transceiver with a range of frequency of 284-960 MHz, which includes several bands specially devoted to space communications. Its electrical parameters are operational current of 18 mA and voltage of 3.6 V, thus allowing a low power consumption of 0.065 W. Additionally, the max transmission data rate is 500 kbps, and the operation temperature range is of –40 to +85 ºC. Moreover, Automatic Frequency control, and Automatic gain control are introduced in this model (Silicon Labs,2014). This model exterior view can be seen in Figure 2.6 and detailed parameters in Annex A.

Figure 2.6 Si4455 transmitter (Silicon Labs,2014).

2.2.6. Primary battery.

This is a vital part of the payload as it provides power supply to all modules mentioned above. Given the spherical shape of the satellite, it is not suitable to use solar cells. Among a wide range of available ready-to-use options, the TL 5920 iXtra Series from the Tadiran company can be chosen. This long-term, high-performance battery, using lithium thionyl chloride cells, provides a voltage and capacity are 3.6 V and 8.5 Ah respectively. Also, it efficiently operates in a wide temperature range of –55 to +85 ºC. Moreover, its mass is 49.5 g with 26 mm width and 50 mm length. The remaining cell features can be found in Annex A, where we include the data sheet from the provider (Tadiran, 2012). Figure 2.7 shows its exterior view.

Figure 2.7 Primary battery TL 5920 iXtra (Tadiran, 2012).

2.2.7. Structure.

These assembly of electronic devices will be embedded inside silica aerogel from the High Tech Material Solutions whose properties are shown in Figure 2.8. The purpose of the embedding aerogel is to thermally isolate, due to its extremely low thermal conductivity, the payload from exterior conditions. This surprising material also has a very low density of about 0.1 grams per cubic centimeter and, yet, has a significant mechanical resistance. To help with the passive thermal control and additional protection from atomic oxygen effect and aerodynamic heating, this aerogel will be covered by a thin layer of space qualified plastic. Furthermore, this material has flight heritage, as it has been used as electronic insulator in Mars roves and as a collector of cometary and interstellar dust in the Stardust mission.

Figure 2.8 Silica aerogel in different configurations (HighTechMaterialSolutions, 2020).

Silica aerogels demonstrates features that cannot be compared to other materials. Due to its very low density and thermal conductivity, aerogel is considered as the best material with high thermal insulation for femtosatellites. Table 2.1, retrieved from the manufacturer website, provides many other physical properties of the aerogel (HighTechMaterialSolutions, 2020).

Table 2.1 Aerogel physical properties.

Properties	Value
Density	0.1 (0.3 - 0.05) g/cm^3
Dielectric constant	1.02 - 1.48 (20 GHz)
Surface Area, BET	800 m^2/g
Percent solids	0.5 - 14%
Mean pore diameter	≈20 nm
Primary particle diameter	2 - 5 nm
Index of refraction	1.002 – 1.063
Thermal tolerance	to 500°C
Poisson's ratio	0.24
Young's modulus	10 MPa – 0.1 MPa
Tensile strength	16 kPa
Fracture toughness	0.8 kPa*m$^{1/2}$
Compression module	0.3 MPa
Thermal conductivity in air	0.016 W/m*K
Thermal conductivity in vacuum	0.004 W/m*K
Sound velocity through the medium	< 200 m/sec
Transparency	>90% visible wavelengths

2.2.8. Summary of the femtosatellite budgets.

Table 2.2 summarizes the key parameters of the femtosatellite such as mass, power, voltage, current and operation temperature ranges.

Table 2.2 Summary of the devices.

Module	Mass, g	Voltage, V	Current, mA	Power, W	Operation temperature, ºC
Accelerometer	2	32	10.5	0.036	– 55 to + 125
GNSS receiver	1	3.3	15	0.05	– 40 to + 85
Microprocessor	3	3	0.6	0.002	– 40 to + 125
Flash memory	1	3.6	8	0.029	– 40 to + 85
Transmitter	2	3.6	18	0.065	– 40 to + 85
Battery	49.5	3.6	-	-	– 55 to + 85
	57.5	49.1	52.1	0.182	

The mass of aerogel will depend on the volume of the femtosatellite. If the femtosatellite has a radius of 5 cm, which is our baseline choice, the volume will be 524 cubic centimeters, and then the total mass will add to 99.9 grams.

2.3. Samara Design.

This project is a collaboration with the Inter-University Department of Space Research of the University of Samara. The Russian design significantly differs from our design; the most salient variation is related to the attitude determination. In our case, attitude is not controlled, which forces us to employ three 1D accelerometers at right angles. Aerodynamic stabilization aligns the satellite with the direction of the ram flow (the rarefied gas impacting on the satellite). This stabilization is obtained by separating the center of mass from the geometric center of the satellite. In this case as it can be seen in the figure below, the satellite aligns with the residual atmosphere along the axis determined by the line uniting the geometric center and the center of mass, producing a coefficient due to the aerodynamic restoring moment given by (Belokonov et al., 2019)

$$a(H) = a_0 \, S \, l \, q(H)/J \tag{2.3}$$

where a_0 for a CubeSat is

$$a_0 = -4C_D k \, \Delta\bar{x}/\pi \tag{2.4}$$

being $C_D = 2.2$ the aerodynamic drag coefficient, k the ratio of a lateral side area to the total area, and

$$\Delta\bar{x} = \frac{\Delta x}{l} \tag{2.5}$$

with Δx the distance from the center of mass to the geometric center and l a characteristic dimension of the satellite. S, H, and J are, respectively, the cross-section of the satellite, the orbital height and the inertia moment along the axis containing the geometric center and the center of mass.

Besides requiring less accelerometers, this configuration also reduces the problem associated with the rotation of the satellite. In our configuration it would be necessary to measure the centrifugal acceleration (in the non-inertial, rotating reference system attached to the satellite) to subtract it. This procedure is possible, but could potentially reduce the sensitivity of the accelerometer.

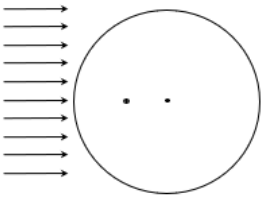

Figure 2.9 The center of mass (crossed circle) at a distance $\boldsymbol{l}$ of the geometric center (solid circle) determines an aerodynamic torque that can be used for attitude control.

Chapter 3

ORBIT ANALYSIS AND SELECTION.

In this chapter of the project we will present a preliminary orbital mechanics analysis of the femtosatellites swarm and available options for its launch. Moreover, the orbit analysis of femtosatellite with different physical properties such mass, radius and drag coefficient will be considered from the simulation results made using the DRAMA software tool developed by ESA.

3.1. Suitable Orbits.

According to the mission's operation height requirement of 300 km above the ground, the swarm orbit is referred to as a very low Earth orbit (vLEO). Besides the basic requirement of being inside the lower thermosphere, we can highlight several key benefits of this particular orbit selection; the first one is that the satellite - ground link is very short, thus resulting in very low values of path losses that allows the use of a relatively small antenna system with lower gain. In order to comply with the requirement of covering the whole thermosphere (including polar regions) our choice of inclination will be 90 degrees. At this high inclination, the launched femtosatellites pass across high latitudes (Ippolito, 2008). A very similar orbit implementation can be found in many remote sensing and space weather study missions, although in these cases the inclination is in the range of 92 – 97 degrees in order to achieve a Sun-synchronous orbit. Figure 3.1 illustrates the femtosatellite trajectory on polar orbit.

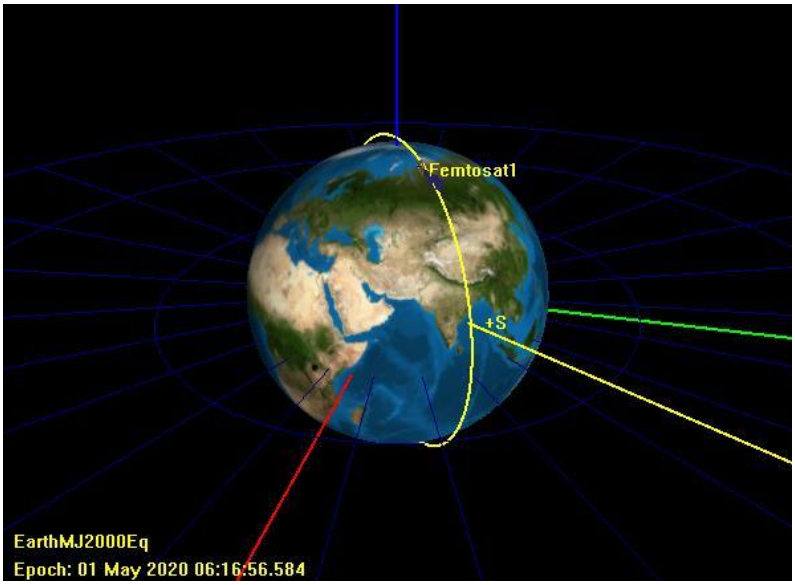

Figure 3.1 View of the polar orbit (obtained with GMAT).

Table 3.1 summarises the orbital elements of the chosen inclined polar orbit.

Table 3.1 Selected orbit parameters.

Element	Semi-major axis (a)	Eccentricity (e)	Inclination, (i)
Value	6680 km	0	90°

The orbital period can be determined using the femtosatellites orbital elements by means of

$$P = 2\pi\sqrt{\frac{a^3}{\mu}} = 90.5 \text{ minutes} \quad \textbf{(3.1)}$$

where a is semi major axis, and μ is the Earth's gravitational parameter equal to $GM_E = 3.9866 \times 10^{14}\ \mathrm{m^3 s^{-2}}$.

For this orbital period of the satellite the number of orbits per day can be estimated to be about 16 (to be more accurate, it is 15.9). The ground track of the designed orbit with inclination of 90° and right ascension of the ascending node (RAAN) of 0° for one femtosatellite can be seen in the figure below. Note that even if we have stated that 90° is the chosen inclination, it is likely that the test-of-concept demonstrator will be launched as a secondary payload, and the Sun-synchronous orbits will be a likely destination. In this case, we would not be able to study the polar caps.

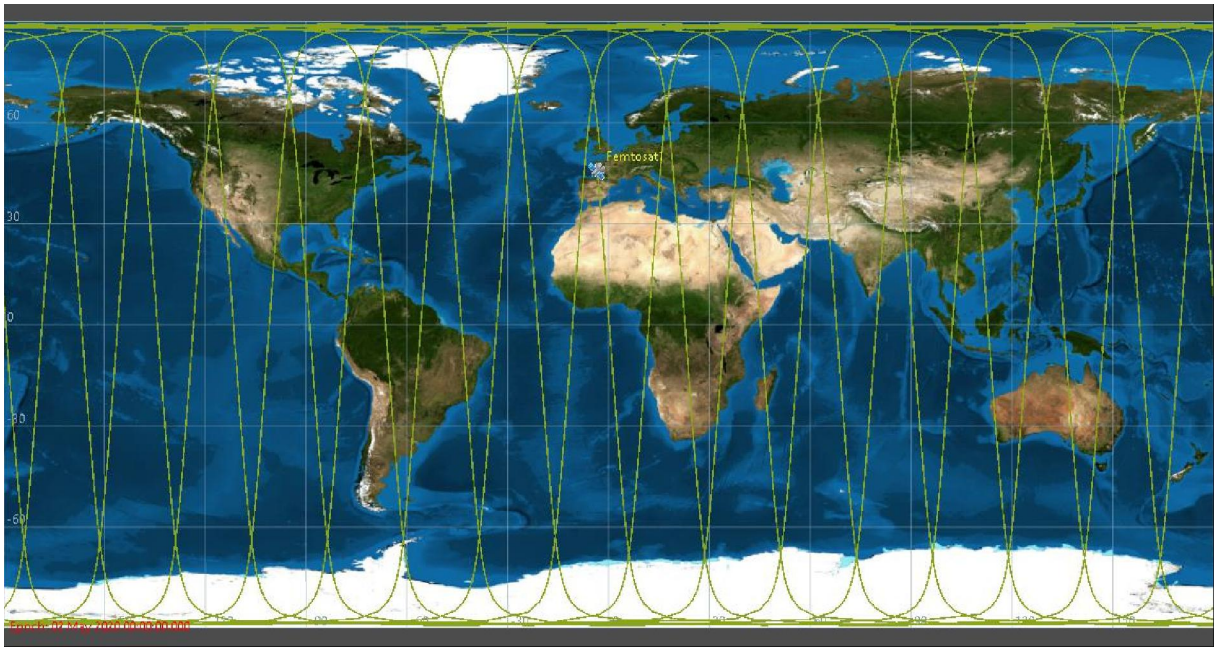

Figure 3.2 Ground track of one femtosatellites with $\boldsymbol{i = 90°}$ (obtained with GMAT).

The illustrated ground track plot was obtained with the *General Mission Analysis Tool* software which is developed by NASA (https://software.nasa.gov/software/GSC-16228-1).

The deployment of the swarm of femtosatellites into the chosen orbit from the launcher as a secondary payload seems to be the most feasible technique. This technique is also called *piggyback* and is provided by several launch providers working for NASA, ESA, JAXA or private corporations. Depending on the launcher, a rideshare can allow the launch of up to 200 kg for secondary payload at a reduced cost, thus opening low-cost launch opportunities for universities and small private companies.

To simultaneously determine the density of the thermosphere over the whole Earth, it would be necessary to use several orbital planes with the femtosatellites distributed on each plane as the pearls in a necklace. Accomplishing this dispersion seems to be a very expensive –and unlikely– option for the secondary payload status of this mission. Spreading out femtosatellites into three different planes separated by a right ascension of the ascending node (RAAN) of 60° is suggested. The figure below shows ground tracks of the femtosatellites in three different orbital planes with inclination of $90°$ but separated by 60 degrees in RAAN.

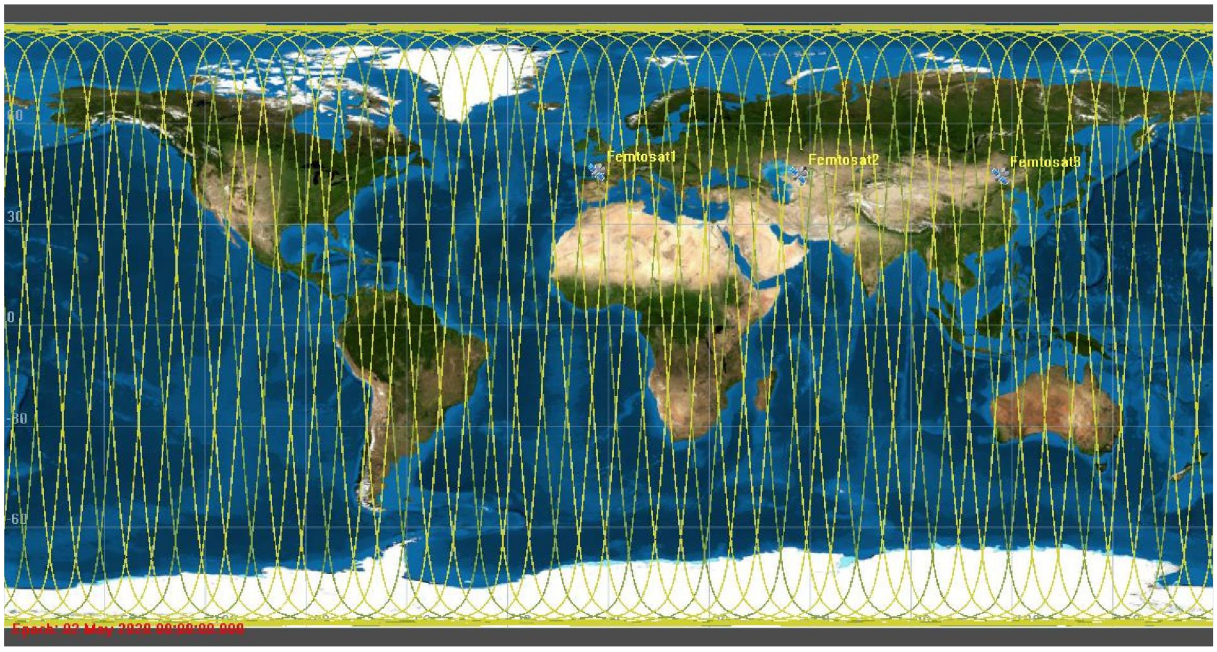

Figure 3.3 The ground tracks of the three femtosatellites constellation with $\boldsymbol{i = 92°}$ (obtained from GMAT).

Coverage map of this three-plane deployment seems to be reasonable in terms of data gathering from multiple locations of thermosphere, but the main issue would be realisation of this deployment from just one launch as our femtosatellites design lacks any kind of orbit control to enable required orbit plane changes. Even if the satellites carried some sort of engine, it would be highly unlikely to obtain the large Δv required for such a manoeuver.

According to Janson and Barnhart (Janson, 2013), there are several methods of implementing orbital changes to be performed by very small satellites based on previous missions. The main idea is to vary the satellite's ballistic coefficient to reduce its altitude and then recovering the original altitude after a period of time, thus resulting in different right ascension of the ascending node (RAAN). This method would allow satellites to move to different orbit planes. The techniques analysed in this case study, however, require active orbit control (i.e., a rocket engine or a propulsive device of some sort) which cannot be implemented in our proposed mission as the satellites' and mission parameters are not comparable. For instance, in the first picosatellite considered by Janson and Barnhardt the total mass is 1.3 kg at an altitude of 780 km, and the satellite counted with deployable wings used to disperse satellites along orbit; in the second case femtosatellites were stored in CubeSats during their RAAN modification phase at altitudes higher than 600 km, resulting in 4 years to establish full constellation (Janson, 2013).

In our proposed mission the ballistic coefficient variation technique to disperse femtosatellites along the polar orbit can potentially be utilised; this technique will be presented in the next section.

3.2. Analysis of the ballistic parameter variations.

As is well known, the main perturbation factor in LEO is the atmospheric drag that reduces the orbit's semi-major axis consequently causing re-entry. Also, solar radiation effects should be mentioned in case of satellites with very low ballistic coefficients.

Assuming a form analogous to the expression of drag for continuum media, we can write

$$D = \frac{1}{2}\rho V^2 S C_D = ma \tag{3.2}$$

where ρ is the atmosphere density, V is the satellite velocity relative to the local atmosphere, S is the satellite cross section area, m is the mass and C_D is the drag coefficient.

We define the ballistic coefficient as

$$B = \frac{m}{SC_D} \tag{3.3}$$

It is clear that changing the value of the ballistic coefficient, we will modify the interaction of the femtosatellite with the thermosphere, and so the acceleration. Provided the lifetime in orbit is long enough, this could cause a dispersion of the femtosatellites having different ballistic coefficients.

To analyse this dispersion mechanism, we employ the simulation tool provided by ESA called *Debris Risk Assessment and Mitigation Analysis* (DRAMA). DRAMA is the

software to analyse a space mission from the point of view of space debris mitigation standards. This software instrument allows to simulate and analyse debris impact flux levels, collision avoidance manoeuvre frequencies for a given spacecraft and risk level, re-orbit and deorbit fuel requirements for a given initial orbit and disposal scenario, cross-section calculation, or re-entry predictions for user defined objects. The specific DRAMA component that is of our interest is the Orbital Spacecraft Removal (OSCAR). Moreover, it allows to simulate different scenarios for solar and geomagnetic activities which are key factors of the specific orbital lifetime. A detailed description can be found in the report in DRAMA final report (2014).

The procedures of the femtosatellites dispersion simulations can be divided into three groups: drag coefficient variation, spherical structure size variation, and mass variation, but actually the relevant changes are those of the ballistic coefficient, irrespective of the cause for them. Then, different values of the ballistic parameter are implemented in OSCAR simulations which allows us to analyse their effect on the femtosatellite's orbit and, consequently, on their lifetime at a given height.

Concerning the femtosatellites dispersion with different drag coefficients (C_D), we simulated femtosatellite operation case for drag coefficients C_D of 2, 2.2 and 2.4 with the sphere radius (*R*) of 5 cm and its mass (*m*) of 100 grams. The results are analysed in the following paragraphs.

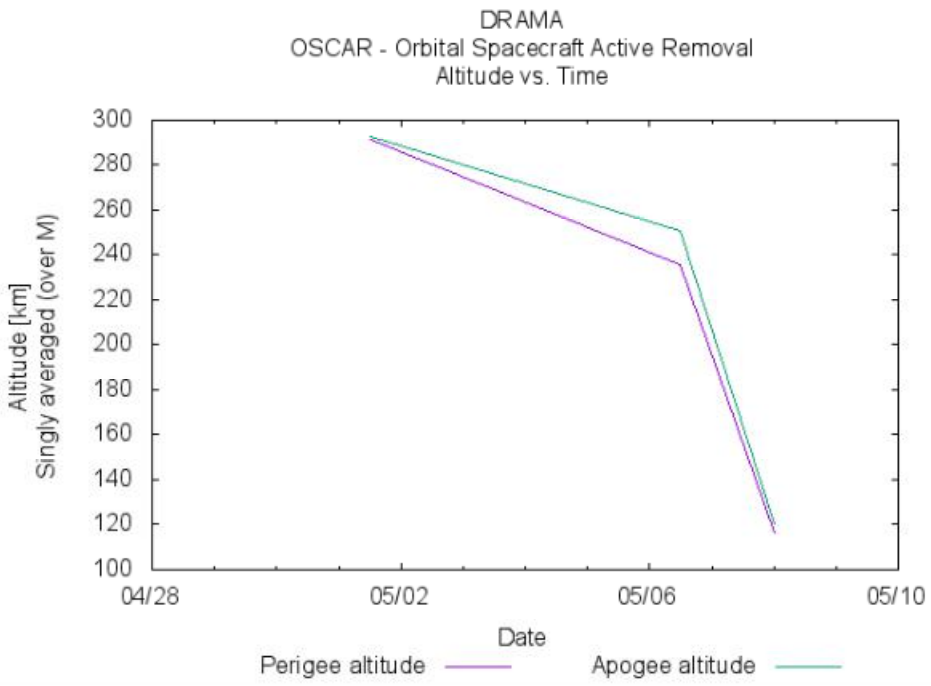

Figure 3.4 C_D of 2 with *R* of 5 cm and *m* of 100 grams.

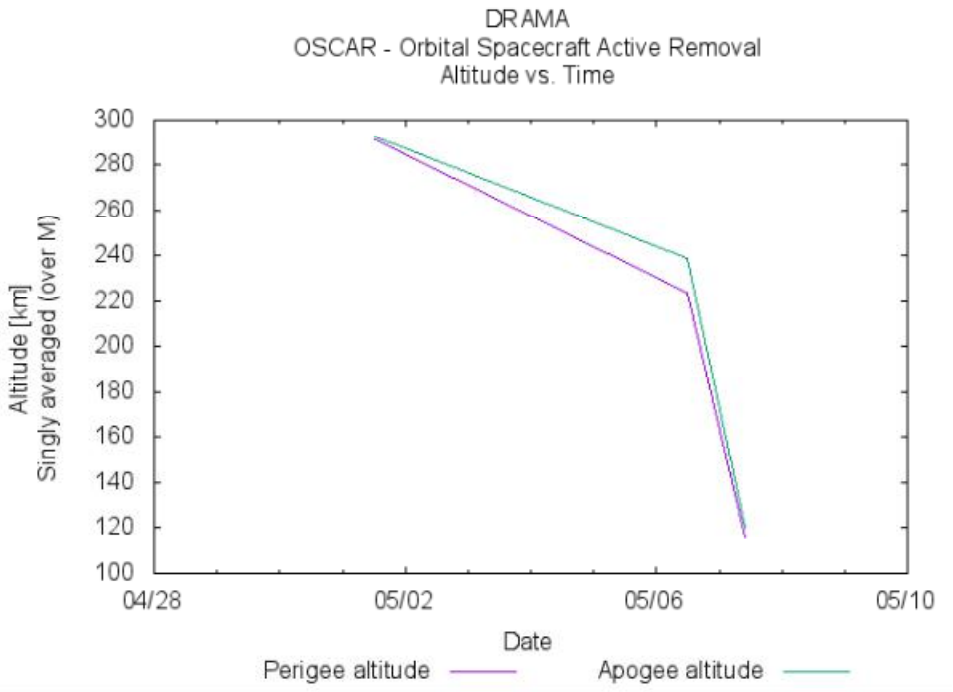

Figure 3.5 C_D of 2.2 with *R* of 5 cm and *m* of 100 grams.

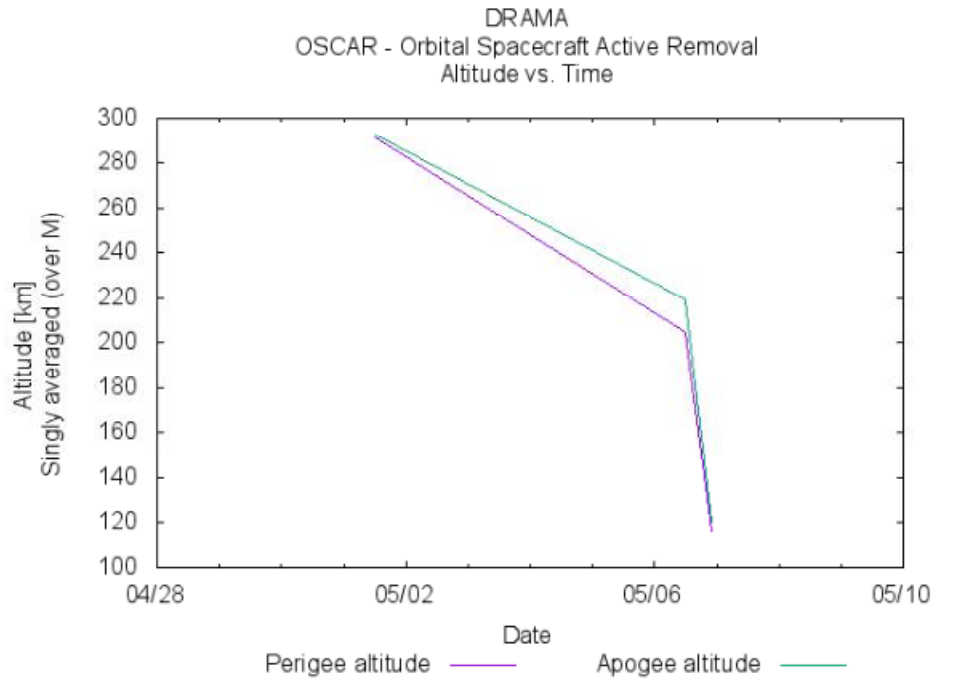

Figure 3.6 C_D of 2.2 with *R* of 5 cm and *m* of 100 grams.

Each of these graphs shows the decrease tendency of orbital lifetime as drag coefficient increases (C_D of 2, 2.2 and 2.4 respectively). These results actually prove the point as the ballistic coefficient decrease then femtosatellite falls down faster i.e. it experiences higher drag force.

There are some salient features in these graphs. The first is that, even if the orbit starts being circular (e=0), the difference in density between the dayside and nightside of the Earth causes a slight increase in the eccentricity. This result, correct, is at odds with the usual statement that drag causes the circularization (thus the decrease of e) of the orbit. This is true only as long as the air's density is constant, which is not our case.

A second surprising feature is the sudden break in the slope of the curves. This is obviously an anomalous effect caused by the different numerical models adopted in some circumstances. This is a serious problem, and one that stresses the interest of the mission we are proposing.

Regarding to the femtosatellites dispersion with cross-section variations (*S*), we have explored them by simply increasing their radius (*R* = 5 cm, 10 cm and 20 cm) but with the same drag coefficient (C_D of 2) and mass (*m* of 100 grams). In Figures 3.7 to 3.9 we can identify a similar effect on orbit lifetime as the one found in previous simulations changing drag coefficient.

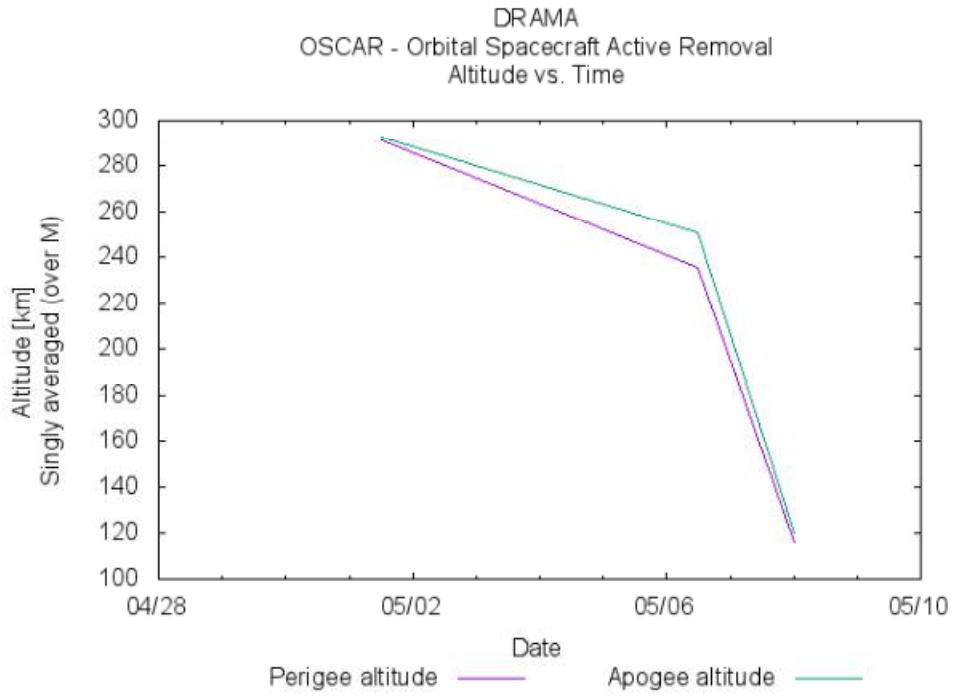

Figure 3.7 *R* of 5 cm with C_D of 2 and *m* of 100 grams.

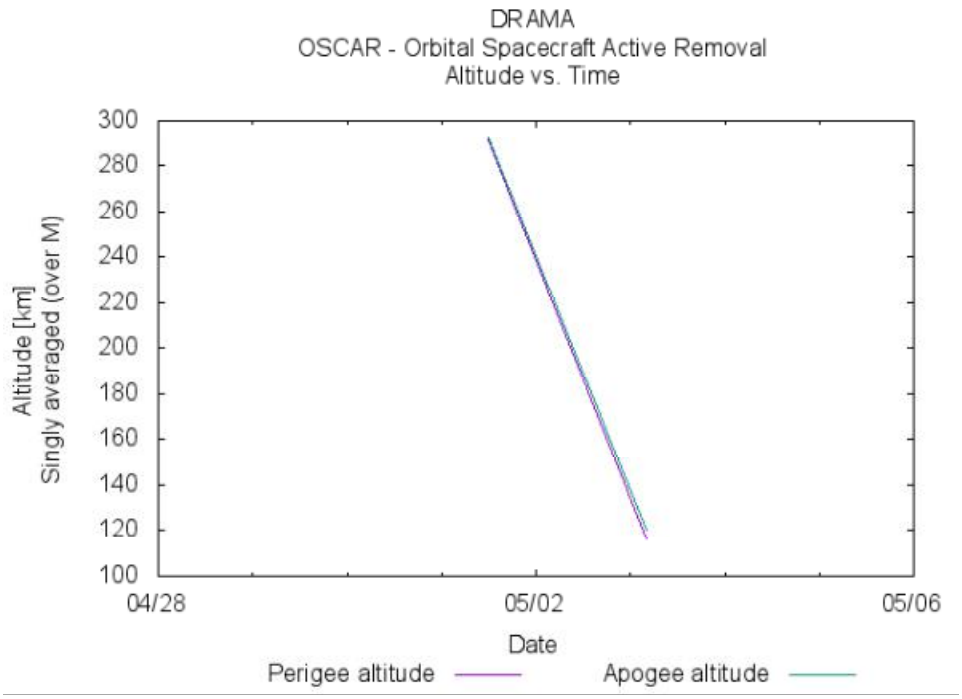

Figure 3.8 *R* of 10 cm with C_D of 2 and *m* of 100 grams.

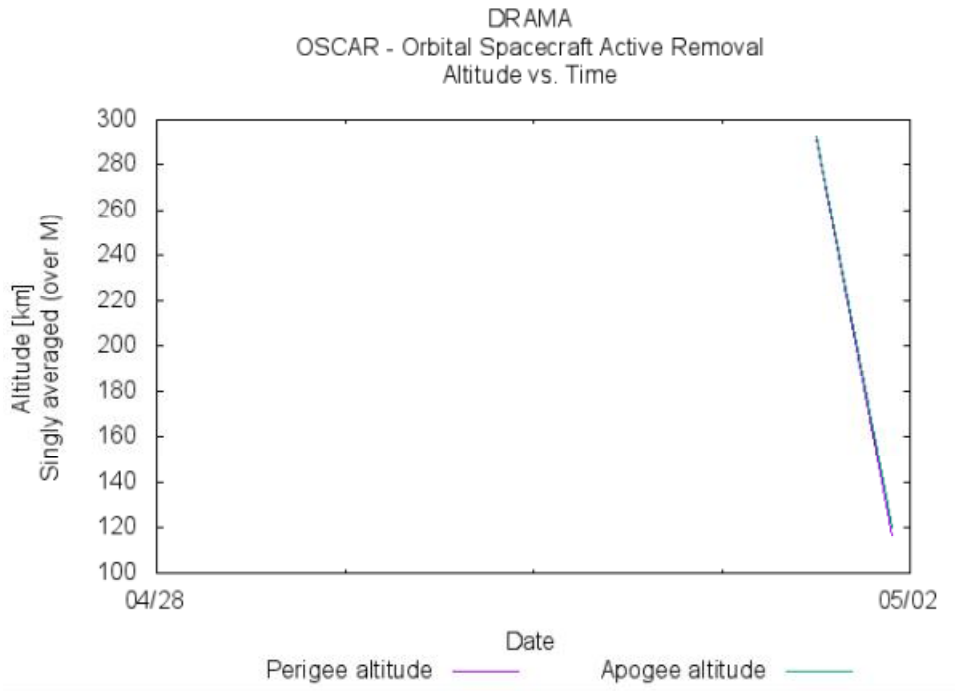

Figure 3.9 *R* of 10 cm with C_D of 2 and *m* of 100 grams

Each of these graphs shows the decrease tendency of orbital lifetime for radiuses (R) of 5 cm, 10 cm and 20 cm respectively. These results eventually state the previous conclusion, as if the ballistic coefficient decreases then the femtosatellite falls down faster, i.e. it experiences higher deceleration.

Finally, regarding to the femtosatellites dispersion with mass variations (*m* of 0.1, 0.2, 0.4, 0.6, 0.8 ad 1 kg) but with the drag coefficient (C_D) of 2 and radius (*R*) of 5 cm, it can be seen that as mass increases, so does the ballistic coefficient, and the deceleration reduces leading for longer orbital lifetime. This tendency is shown in the graphs below for the different masses mentioned above.

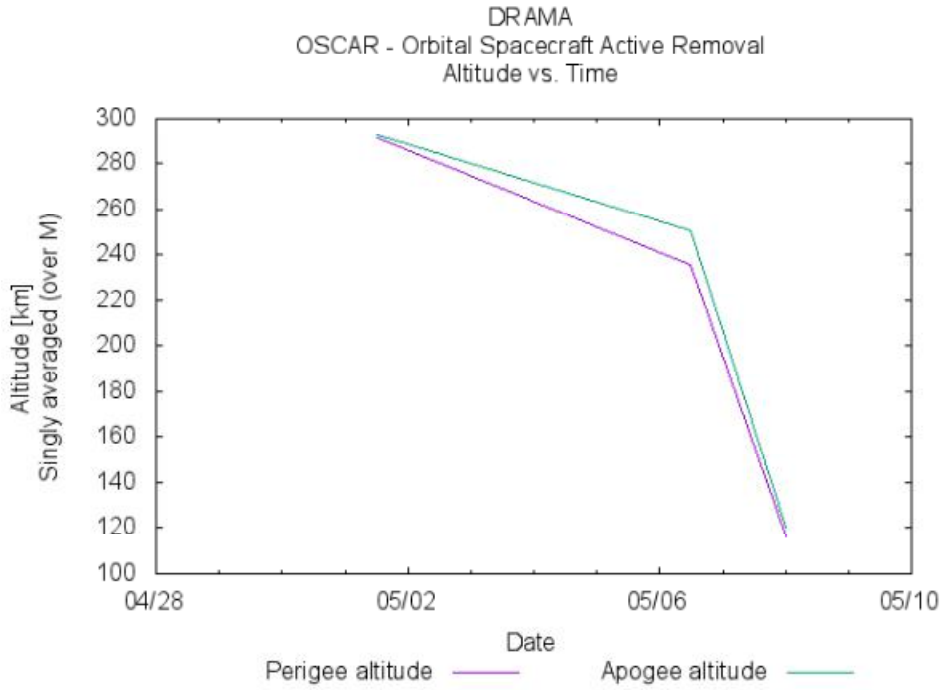

Figure 3.10 *m* of 0.1 kg with C_D of 2 and *R* of 5 cm.

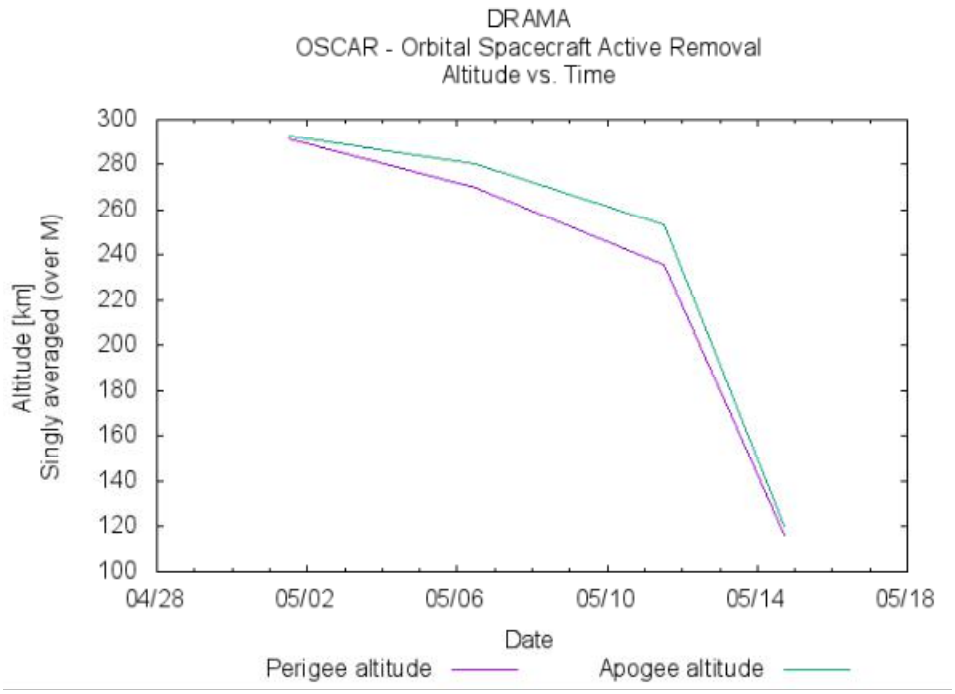

Figure 3.11 *m* of 0.2 kg with C_D of 2 and *R* of 5 cm.

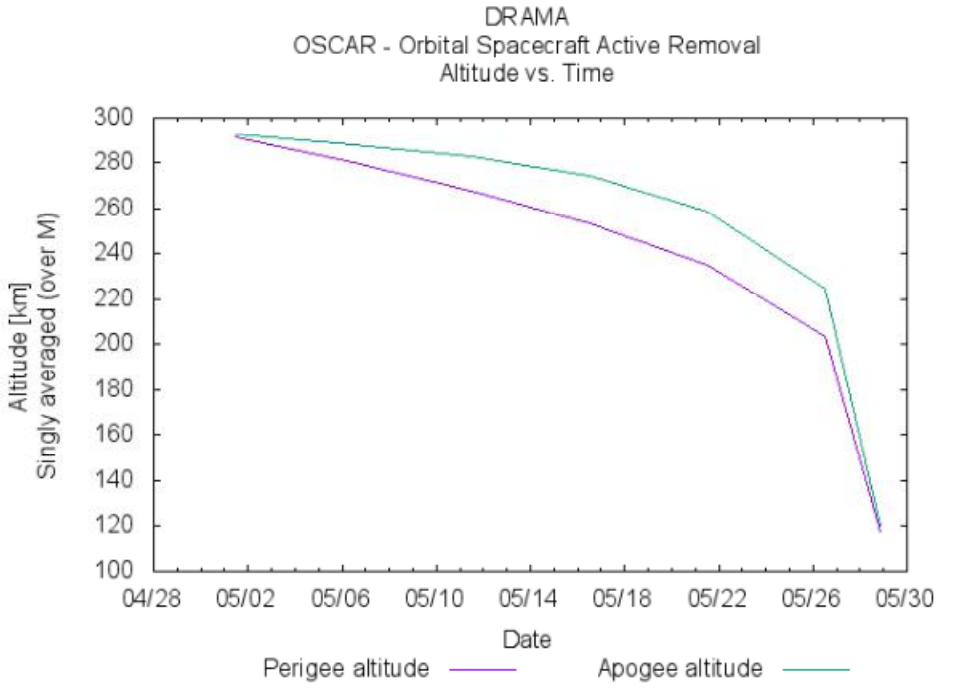

Figure 3.12 *m* of 0.4 kg with C_D of 2 and *R* of 5 cm.

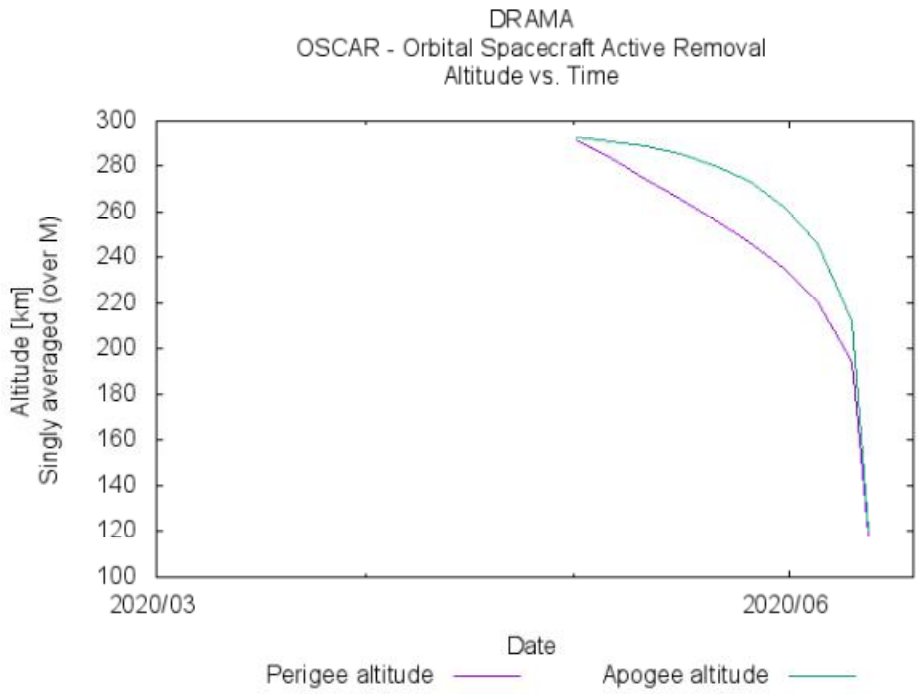

Figure 3.13 *m* of 0.6 kg with C_D of 2 and *R* of 5 cm.

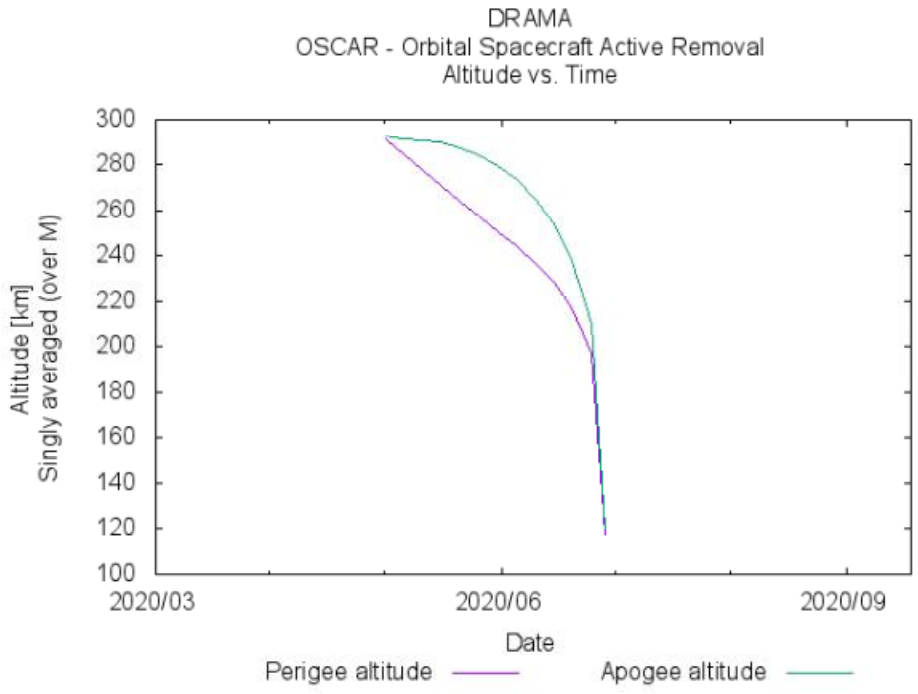

Figure 3.14 *m* of 0.8 kg with C_D of 2 and *R* of 5 cm.

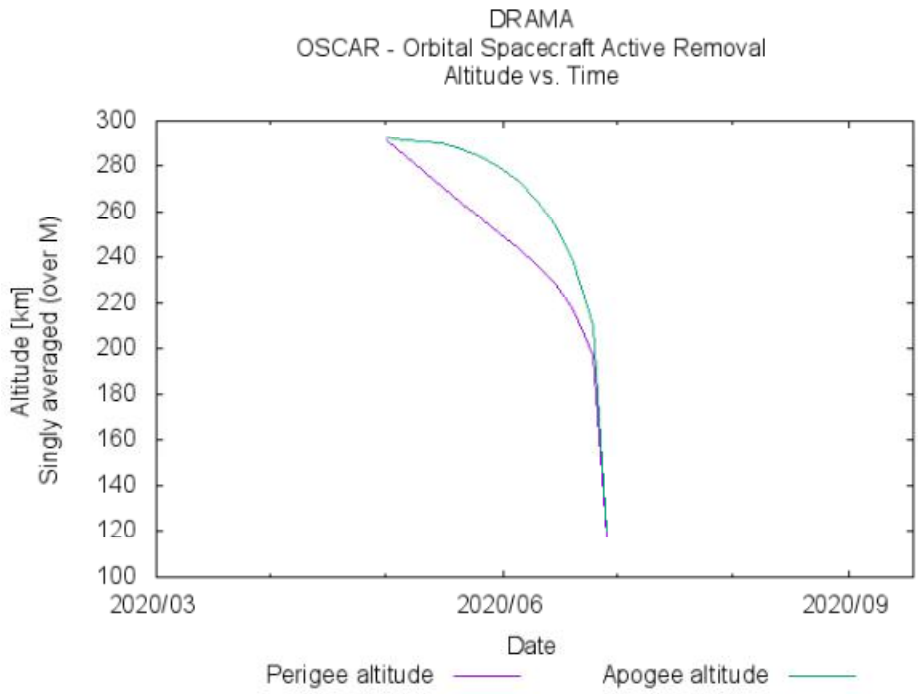

Figure 3.15 *m* of 1 kg with C_D of 2 and *R* of 5 cm.

To summarise the analysis of results obtained by means of the OSCAR simulation tool, it can be stated that varying femtosatellites physical parameters –thus changing ballistic parameter– allows to manage femtosatellites dispersion along selected polar orbit with no propellant requirements.

Nevertheless, as the residence in orbit is around a week in most cases, the dispersion by means of changes in the ballistic coefficient does not seem effective. The characteristic time required for significant dispersion is much longer than the orbital lifetime. Thus, other methods should be investigated.

3.3. Potential Launch Vehicles.

Previous satellite constellations have been deployed in orbit through several launches. The high cost of a single launch in comparison to the significant low cost of small satellite constellation development means that it is not a financially feasible option for universities and small private companies (or even for large companies and research institutions, as the limited lifetime of the mission calls for reduced budgets). Hence, the small constellation is considered as the secondary –even tertiary– payload to be launched as rideshare from a launch vehicle. In this section, the availability of different launchers will be considered and possible launcher options will be selected for our swarm mission.

The relatively low cost of piggyback launches is a benefit for reduced budget missions, but there are severe limitations regarding orbit selection (which is the sole responsibility of the primary payload), long periods of waiting time as the prime

spacecraft launch is obviously the absolute priority, and uneven availability. Furthermore, in most cases a “dead” launch is enforced: the secondary payloads must be completely stopped, in such a way that cannot generate any sort of electromagnetic noise.

At the same time, the deployment assistance technology to store secondary payload during launch and then release them into orbit is well developed in such rockets as SSPS on *Falcon* 9, ASAP on *Soyuz*, VESPA on *Vega*, and ESPA on *Atlas* 5 and *Delta* 4. The only offer for secondary payloads of the micro launch vehicles family is *Pegasus*, with up to 310 kg capacity. Table 3.2 summarises launch vehicles in terms of orbit parameters, capacity, launch and specific costs (Wekerle, 2017).

Table 3.2 List of potential launch vehicles.

Launch Vehicle (organisation, country)	Number of launches / reliabilities	Payload capacity (kg) (altitude x inclination)	Launch price (million USD)	Specific price (USD/kg)
Pegasus XL (Orbital Science Corp, US)	42 / 93%	LEO: 310 (700 km x 70°) SSO: 210 (700 km x 98°)	56.3	181161-268095
PSLV XL (ISRO, India)	35 / 94%	SSO: 1750 (700 km x 98°)	25-35	14285-20000
Rokot (Eurorockot, Europe and Russia)	30 / 90%	LEO: 1580-1840 (700 km x 86.4°-63.2°) SSO: 1350 (700 km x 98°)	35-45	16304-25926
Vega (Arianespace, Europe)	7 / 100%	Polar: 1430 (700 km x 90°) SSO: 1750 (700 km x 98°)	35-45	24476-33834
Soyuz-2 (TsSKB-Progress, Russia)	97 / 92 %	LEO: 7020 SSO: 4230	80	11396-18912
GSLVMk III (ISRO, India)	4 / 100%	LEO: 10000 (660km)	53	5300
Falcon 9 Full Thrust (SpaceX, USA)	59 / 100%	LEO: 22800	50	2192
Atlas V (ULA, USA)	81 / 98%	LEO: 8250 -20520	110	5360-13300
Ariane 5 (Airbus Defence and Space for ESA, Europe)	106 / 95%	LEO: 20000 (260 km x 51.6°)	220	11000

Among all the medium-lift launch vehicle the *Falcon* 9 Full Thrust of SpaceX can be highlighted as primary choice in terms of its excellent reliability and the lowest specific

cost. Moreover, according to SpaceX the *Starlink* mission of small satellites constellation for communication and Internet of the Things applications will open piggyback opportunities in the large series of launches dedicated to this mission. The small launch vehicle *Vega* of Arianespace can be the alternative choice in terms of its launches to polar and sun-synchronous orbit that fulfil our proposed mission requirements, but its seems not financially affordable.

Chapter 4

MISSION ANALYSIS.

In this chapter we analyse the communication architecture as well as thermal, power and mass budgets. Current development state allows only very generic analysis, as the details of every subsystem are still rather uncertain. Nevertheless, this first-order analysis will give an indication of whether the mission is feasible or not.

4.1. Communication architecture.

In our proposed femtosatellite design, measured data are required to be transmitted down to data center without any data compression algorithms. Compression would be used only if it proves necessary, as it causes an overhead of the on-board computer. We propose a communication link for the mission according to the swarm orbit and the selected sensors for the femtosatellite, such as accelerometers and GNSS receiver from which the data will be obtained. In particular, we will determine a first estimation of the satellite-station data downlink, with special focus on the data rates.

As the mission is very short and the satellites are so simple, we do not envision the need for uplink. The only case that would require that would be a mistake on the on-board software; a suitable set of tests, including some demonstration missions, should ensure that no such mistakes are made.

4.1.1. Ground station.

Our first step is to select a suitable ground station. According to the polar orbit of the mission, ground stations located at very high latitudes are the better suited for our purpose. Hence, one ground station in near polar regions is selected for the communication architecture, and the Svalbard Satellite Station (SvalSat) is a particularly suitable facility, being far North. Figure 4.1, created using GMAT (General Mission Analysis Tool, provided by NASA) mission analysis software, illustrates the ground track of one femtosatellite and SvalSat location.

The ground station itself is marked at high north latitude as “GroundStation1” and a symbol containing a parabolic antenna. The fact that the ground station is that far north will increase the number of contacts with the femtosatellites.

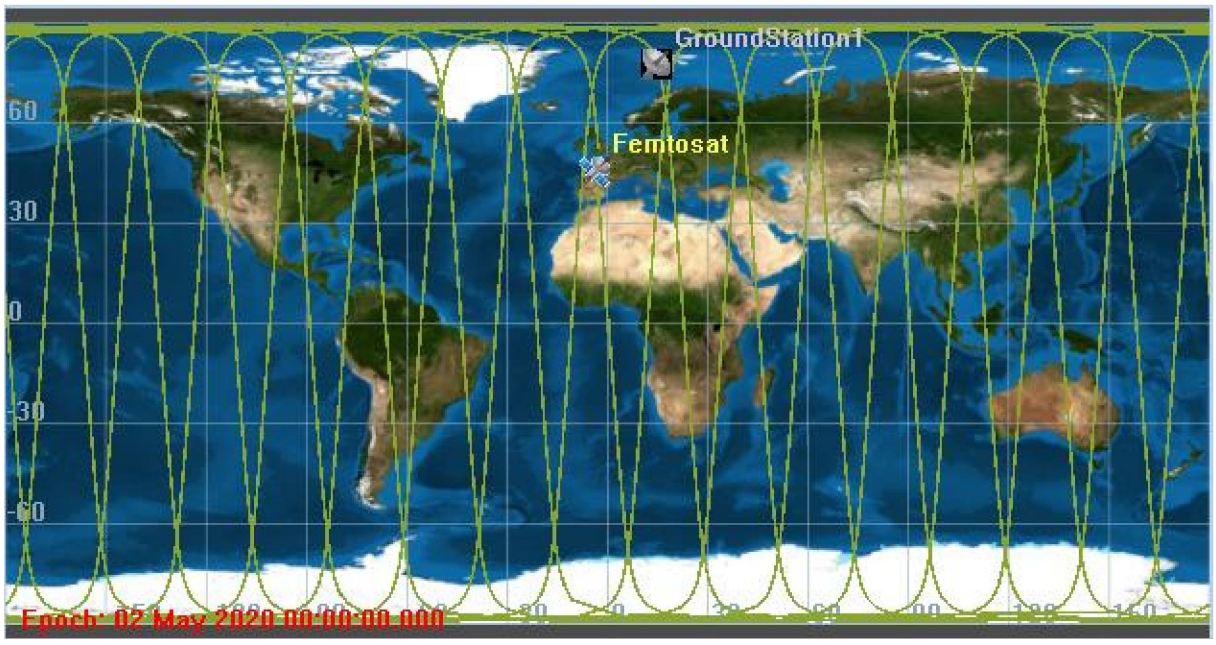

Figure 4.1 Ground track of a femtosatellite in near-polar orbit ($\boldsymbol{i} = \mathbf{92}°$) and Svalbard location.

The SvalSat is the largest commercial satellite ground base located on Spitsbergen island (Norway). Svalbard station that was erected in 1997 and is under control of Kongsberg Satellite Service (KSAT). Together with the ground station in Antarctica, these bases offer unique visibility and contact times for polar orbiting satellites at low heights on every revisit as planet rotates. This facility includes about 30 multi mission antenna systems in a wide range bands such as C-, L-, S- and X-band. This all-orbit-support for polar orbiters is dictated by its extreme north site with coordinates 78.22° N, 15.39° E and an altitude of 500 m above sea level. The number of small customers has increased since 2004 when a fiber optic communication link connected Svalbard to Norway mainland entered into function. It is important to mention that SvalSat is an essential part of NASA's, ESA's, JAXA's and small customers' space mission in terms of communication and command (Svalbardblues.com, 2020).

Figure 4.2 Svalbard ground stations (Svalbard/Facebook).

4.1.2. Data rates.

In order to provide thermosphere density data with high accuracy, it is expected that one measurement will be taken every second (then, some 8 km apart). These measurements include data about the determined accelerations, as well as measures of the temperature of the three single axis accelerometers (which will have an impact on the accelerometer's calibration); position and time from the GNSS receiver will be tied to the acceleration measurements. Table 4.1 summarizes the amount of the gathered bits in every second.

Table 4.1 Data to be measured and associated amount of information in bits.

Data type	Bits	Data accuracy
Acceleration	19	10^{-6} m/s^2
Temperature	15	0.01 K
Location (Cartesian coordinates)	69	2.5 m
Time	30	0.01 s

This results in a total of 133 bits per second, and then the data generated after one complete orbit, that was defined in previous chapter as lasting for 90.5 minutes, can be approximately estimated as –applying an additional margin of a 20% for satellite identification, packet identification, error correcting code information–

$$N = 133\ bits \times 5430\ s \times 1.2\ = 866628\ bit\ or\ 866.63\ kbit \quad \textbf{(4.1)}$$

Hence, the total data generated per one day (24 hours) where satellite orbits the planet 16 times is 13.87 Mbit.

Regarding to the data rate, this value depends on satellites revisits and their time in view of the ground station in one day. These values have been computed using GMAT by simply implementing mission's parameters. The resulting visibility times are found in Table 4.2, and show that there is a total of 3606 seconds of visibility, with an average visibility time of 240 seconds. With this average we obtain a required data rate of 58 kbit/s in order to download the amount of data gathered during a full day.

Table 4.2 Satellite revisit number and its each duration in one day.

Target: Femtosat

Observer: GroundStation1

Start Time (UTC)	Stop Time (UTC)	Duration (s)
01 May 2020 00:03:45.635	01 May 2020 00:09:28.219	342.58397369
01 May 2020 01:35:19.721	01 May 2020 01:39:42.421	262.69998107
01 May 2020 03:07:45.026	01 May 2020 03:09:47.460	122.43401989
01 May 2020 06:11:13.760	01 May 2020 06:12:08.541	54.781717609
01 May 2020 07:41:02.383	01 May 2020 07:44:48.584	226.20116413
01 May 2020 09:11:07.698	01 May 2020 09:16:26.301	318.60313446
01 May 2020 10:41:13.308	01 May 2020 10:47:07.978	354.67029606
01 May 2020 12:11:17.394	01 May 2020 12:16:53.581	336.18688728
01 May 2020 13:41:18.908	01 May 2020 13:45:48.777	269.86841024
01 May 2020 15:11:15.299	01 May 2020 15:14:06.665	171.36630326
01 May 2020 16:40:49.530	01 May 2020 16:42:20.539	91.008983832
01 May 2020 18:09:12.312	01 May 2020 18:11:39.876	147.56363427
01 May 2020 19:37:20.910	01 May 2020 19:41:27.799	246.88816656
01 May 2020 21:05:58.902	01 May 2020 21:11:17.506	318.60395578
01 May 2020 22:35:21.374	01 May 2020 22:41:05.120	343.74648782

Number of events : 15

4.1.3. Link budget.

According to Larson and Wertz (1999), the relationship between the transmitter power, the transmitting and receiving antenna gains, propagation path length and data rate is defined by the link equation or link budget

$$\frac{E_b}{N_0} = \frac{PL_l G_t L_s L_a G_r}{kT_s R} \tag{4.2}$$

where E_b/N_0 is the received energy per bit to noise density ratio, P is the transmitter power, L_l L_s L_a are transmitter to antenna loss, space loss and transmission pass loss respectively, G_t and G_r are gains of transmitting and receiving antennas, k is Boltzmann's constant, T_s is the system noise temperature and R is the data rate.

The link equation (4.2) can be rewritten in decibels as

$$\frac{E_b}{N_0} = P + L_l + G_t + L_{pr} + L_s + L_a + G_r + 10logk + 10logT_s - 10logR \quad \textbf{(4.3)}$$

In general, an E_b/N_0 ratio of 5-10 dB is the minimum requirement to receive binary data with low probability of error, assuming error correction methods. The table below illustrates this bit error probability as a function of E_b/N_0 for several modulation techniques (Larson,1999).

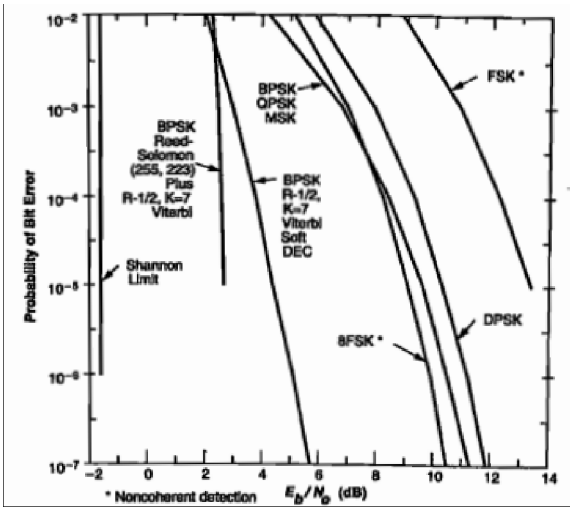

Figure 4.3 BER as function of E_b/N_0 (Larson, 1999).

According to this, with Binary Phase Shift Keying (BPSK) modulation the adequate requirement for E_b/N_0 is 5 dB with a probability bit error of 10^{-6}. Hence, the link budget design can be analyzed using this value. To do so, we need to determine the still unknown parameters of communication link: G_t G_r and L_s whereas defined parameters are listed in Table 4.3.

Table 4.3 Predefined parameters.

Parameter	Symbol	Units	Value
Frequency	*f*	MHz	960
Transmitter power	*P*	dBW	-17
Transmitter line loss	L_l	dB	0
Free space loss	L_l	dB	-141.63
Transmitter gain	G_t	dBi	0
Propagation and polarization loss	L_a	dB	-0.3
Receive antenna pointing loss	L_{pr}	dB	-0.3
Receiver antenna diameter	D_r	m	11
Propagation path length	*S*	m	3×10^5
System noise temperature	T_s	K	300
Data rate	*R*	bits/s	5.8×10^4
Bit error rate	*BER*	-	10^{-6}
Required E_b/N_0	*Req* E_b/N_0	dB	13

Regarding to unknown G_t G_r and L_s, these can be calculated by following equations

$$G = \frac{\pi^2 D^2 f \eta}{c} \text{ or } G = -159.59 + 20\log(D) + 20\log(f) + 20\log(\eta) \quad \textbf{(4.4)}$$

and

$$L_S = \left(\frac{c}{4\pi S f}\right)^2 \text{ or } L_S = 147.55 - 20\log(S) - 20\log(f) \quad \textbf{(4.5)}$$

where *c* is the light speed 3x10^8 m/s, η is antenna efficiency assumed to be 0.5, in the low end of antenna efficiencies. Regarding the gain of the transmitting antenna, as the femtosatellite will not be able to control its attitude and then to point an antenna, we assume that it is isotropic and then has a gain of 0 dB. Finally, the slant range for spatial losses is taken as 1000 km, which is a slight overestimation of its maximum value.

Consequently, these calculated values can be added to the link equation in order to determine E_b/N_0 for our communication link.

Parameter	Symbol	Units	Value
Receiver antenna gain	G_r	dBi	38.38
E_b/N_0	E_b/N_0	dB	24.42
Margin		dB	14.42

To conclude link budget analysis, it can be stated that the determined E_b/N_0 of 24.42 dB indicates a very good quality of our communication link, with a margin of 14.42 dB over than required E_b/N_0 with the BER of 10^{-6}.

4.2. Thermal budget.

In this section we perform a very simple analysis of thermal budget, the so-called single thermal node analysis. Given the extremely limited resources of the femtosatellite, thermal control must be passive. For the analysis of the femtosatellites' operation for hot and cold cases the following thermal balance equation is utilized

$$A_{SC}\varepsilon\sigma T^4 = A_{Sun}\alpha I_{Sun} + A_{Earth}a\alpha IF + A_{Earth}\varepsilon I_{Earth}F + Q_{diss} \quad \textbf{(4.6)}$$

where A_{sc} is the satellite total area (spherical), A_s is the Sun-illuminated cross-section area, A_p is the Earth-irradiated area, I_{Sun} the solar flux (1366 W/m2, I_{Earth} is the Earth emitted infrared flux (237 W/m^2), a the albedo of the Earth (average value 0.3), *F* the visibility factor of the Earth, σ the Stefan-Boltzmann's constant, *Q* the dissipated power in the femtosatellite (which for this analysis can be considered negligible), ε and α are emissivity and absorptivity coefficients, respectively.

According to the values listed in the table below, we can estimate the temperatures for hot (continuous sunlight) and cold (continuous eclipse) operation cases.

Table 4.4 Predefined parameters.

Parameter	Symbol	Value, (units)
Total area	A_{sc}	0.031 m^2
Illuminated areas	$A_{sun}=A_{earth}$	0.00785 m^2
Albedo	a	0.3
Solar flux	I_{sun}	1366 W/m^2
Earth irradiance	I_{earth}	237 W/m^2
Stefan-Boltzmann's constant	σ	5.67×10^{-8} W/m^2K
Emissivity	ε	0.08
Absorptivity	α	0.05

We consider several values for α and ε, and, as stated before, we make the assumption that the dissipated power inside the satellite is 0 W (negligible in comparison with solar, albedo and infrared planet fluxes) and visibility factor of the Earth is 1.

The hot case operation temperature (in sunlight) results in an equilibrium temperature of 327 K (54 ºC), which can be estimated from the expression

$$T^4 = (A_{Sun}\alpha I_{Sun} + A_{Earth}a\alpha IF + A_{Earth}\varepsilon I_{Earth}F)/A_{SC}\varepsilon\sigma \quad \textbf{(4.7)}$$

On the other hand, the cold case operation temperature (in eclipse, where is no solar and albedo flux rates) results in a very low temperature of 180 K (–92 ºC) from

$$T^4 = A_{Earth}\varepsilon I_{Earth}F/A_{SC}\varepsilon\sigma \quad \textbf{(4.8)}$$

Nevertheless, this low temperature is an extreme worse case, as it assumes that the satellite spends an infinite time in darkness, which is a non-realistic situation. This value is just an indication that more detailed calculations must be done. In reality, the femtosatellite operates in a very dynamic environment where it experiences different radiation fluxes in different location and times during its orbital motion.

Table 4.5 summaries required operational temperatures for each module of femtosatellites.

Table 4.5 Operational temperature rates.

Module	Operation temperature, ºC
Accelerometer	– 55 to + 125
GNSS receiver	– 40 to + 85
Microprocessor	– 40 to + 125
Flash memory	– 40 to + 85
Transmitter	– 40 to + 85
Battery	– 55 to + 85

4.3. Power and mass budgets.

Our design of the femtosatellite is based on Commercial-off-the-shelf (COTS) Microelectromechanical Systems (MEMS) devices. In Table 4.5, we list the masses and power requirements of the devices we have selected for the current configuration.

Table 4.6 Power and mass summary of selected devices.

Module	Power, W	Mass, g
Accelerometer	0.036	2
GNSS receiver	0.05	1
Microprocessor	0.002	3
Flash memory	0.029	1
Transmitter	0.065	2
Battery	-	49.5
Total	0.182	57.5

The selected battery lifetime determines the time that the femtosatellite can operate in orbit. Our choice for the battery is the TL 5920 iXtra Series from the *Tadiran*, which features a voltage and capacity of 3.6V and 8.5 Ah, respectively. Then, we can compute its energy as

$$E_b = V \times Q \tag{4.9}$$

This results in a stored energy of 30.6 Wh. Consequently, the time in which the battery will be depleted due to the power consumption during operations can be estimated from

$$E_b = P \times t \tag{4.10}$$

that results in 168.13 hours (just 7 days) when the femtosatellite is in active state. For the last figure we have considered that the femtosatellite is using its transmitter just for 6 minutes every orbit, and during the rest of time it is in sleep mode. This time, if short, is almost equal to the residence time of the femtosatellite before it reenters the atmosphere due to the atmospheric drag, and so we can consider that it is just enough for our purposes. Nevertheless, it would be interesting to count with some margin in this regard.

Chapter 5

DATA ANALYSIS.

In this chapter, we will present the techniques to directly determine thermospheric density and generate the data conducing to refinements in current empirical models. These data can be gathered by several means: our primary choice will be the use of the three onboard single axis accelerometers, but as a backup in case the accelerometers fail, we could use the GNSS receiver navigation solutions, that would allow the orbit reconstruction, and then the determination of an average density. Finally, if the satellite experiences a complete failure, we could still use the data obtained from the ground by several systems that track Earth orbiting objects and produce Two Line Elements (hereafter referred to as TLEs).

The following sections describes each data analysis technique for thermospheric density determination.

5.1. Density determination from accelerometers.

For 50 years or more, onboard accelerometers have been used as a method for density determination and wind estimation, and, in doing so, have provided a unique access to extremely relevant thermospheric data for space and climate science and weather forecasting services. In this particular technique the main aim is to remove radiation pressure models of the Sun and the Earth from measured non-gravitational accelerations and to implement the drag-force equation resulting in density computation.

Among the wide range of type of measurements from instruments provided by several scientific missions, measurements from some of them are particularly useful for density determination. For instance, *CHAMP* (2000-1010), *GOCE* (2009-2013) and *GRACE* (2002-2017) satellites on LEO had the main purpose of determining with exquisite precision the shape of Earth's gravity field. Even if the satellites were not primarily focused on the problem we are analyzing, all of them have been used to study the thermosphere, as the measured non gravitational accelerations by accelerometers carried onboard of these spacecrafts provided accurate and continuous valuable data on drag of exceptional detail and ample coverage. The physical mechanism for these accelerometers consists in measuring the force required to sustain a proof mass at the mass center of the satellite where the gravity force is balanced by centrifugal force (in the satellite-bound non-inertial reference system). Positive and negative drive voltages flow to electrodes with respect to the proof mass's opposite sides, whose electrical potential is maintained at a direct current biasing voltage (Jin, 2018).

The direct data processing in this technique is quite straight forward and the case study of *CHAMP* satellite will be analyzed in the following paragraphs. Figure 5.1 defines spacecraft body fixed (SBF) axes where its velocity and ground pointing directions are the X- and Z- axes, respectively.

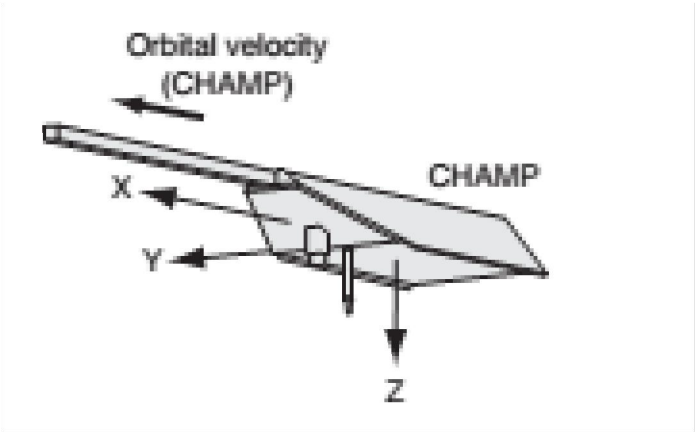

Figure 5.1 SBF axes for CHAMP (Doornbos, 2011).

In the *CHAMP* satellite, the arrangement of accelerometers is mounted close to its mass center and in such a way that their three-axis orientation reference system is aligned to the SBF axes. The active attitude control of *CHAMP* keeps these axes with very small angle variation of the orbit-fixed directions (along-track, cross-track, and radial directions); these angles are defined as roll, pitch and yaw Euler angles for X-, Y- and Z- axes respectively. Hence, due to that small angle variations, the orbital velocity is aligned with X_{SBF} axis and consequently accelerations in that direction are significantly larger than accelerations in perpendicular directions. This method results in an approach for density determination based on using only the acceleration projection on X_{SBF} axis, as is shown in Figure 5.2.

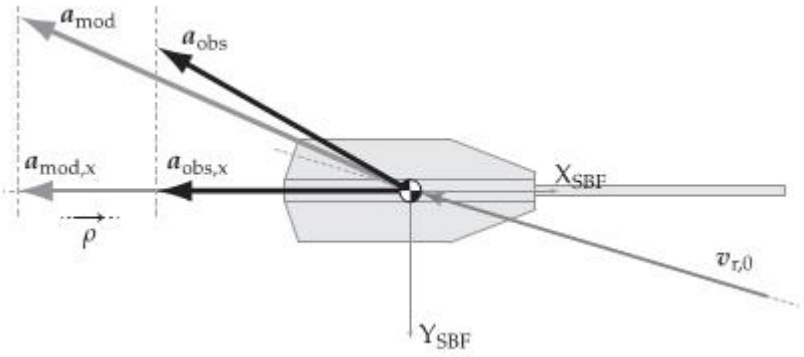

Figure 5.2 Acceleration projection on X_{SBF} axis (Doornbos, 2011).

Then, from the full vector from equation of the modelled acceleration

$$a_{mod} = \frac{1}{2}\rho V_r^2 \frac{SC_D}{m} \quad \textbf{(5.1)}$$

and the density is computed directly from the X-component of vector equation (5.1)

$$\rho = \frac{2ma_{obs,X}}{SC_D V_r^2} \quad \textbf{(5.2)}$$

where a_{obs} is the observed acceleration obtained from raw accelerometer data after removing modelled accelerations due to solar radiation pressure, terrestrial infrared and albedo radiation (Sutton, 2007), and is defined as

$$a_{obs} = a_{raw} - a_{srp} - a_{IR} - a_{alb} \quad \textbf{(5.3)}$$

Sutton (2007) describes another method, the so-called dual axis method, where the point consists in neglecting the sideways and lift forces, or they are modelled and removed from acceleration, and hence the only remaining observed acceleration is due to drag. So, acceleration and density are defined according to Equations 6.1 and 6.2. This a_{mod} vector is decomposed into drag and perpendicular sideways plus lift force components, where the drag component is subtracted from original modelled acceleration, resulting in

$$a_{mod,L} = a_{mod} - a_{mod,D} \quad \textbf{(5.4)}$$

Moreover, data from the cross track and radial directions (Y_{SBF}- and Z_{SBF}- axes) can be used to extract measurements of the wind speed in thermosphere. Even if the air density is very low, thermospheric winds can be faster than 400 m/s, and thus can produce measurable accelerations.

The accuracy of the models can be assessed by comparing the density obtained using this algorithm (ρ) with the prediction of the models (ρ_m); a suitable way is by determining the density residuals

$$r_\rho = \frac{\rho - \rho_m}{\rho_m} \times 100\% \quad \textbf{(5.5)}$$

During conditions of high solar or geomagnetic activity, these differences can range from a 30 to a 200%

5.2. Density determination using a GNSS receiver.

Another technique to derive non-gravitational accelerations is by means of precise orbit ephemeris (POE) derived from GNSS receiver data and its comparison with precise orbit determination (POD) obtained by optical or radar systems. This method provides additional accuracy on data and hence it is used for accelerometers calibration. In case of accelerometers failure, it is considered as a reliable backup tool for measurements (Jin, 2018).

In the last years, several studies (such as those from Kuang et al 2014, Calabia et al 2015 and McLaughlin et al 2012) provided analysis of measured non-gravitational accelerations and the derived densities through precise orbit determination POD obtained by means of the use of the GNSS receiver onboard the satellite. The purpose of these studies is to feature the utilization of the precise orbit ephemeris (POE) to produce corrections for updating current empirical models and, hence, provide more accurate density estimations required for air drag calculation and advanced orbit prediction and determination.

Kuang developed an approach where non-gravitational accelerations and inferred mass densities in thermosphere are computed by estimating the stochastic accelerations that compensate for the dynamic model errors in the reduced dynamic POD. The along-track direction of the circular orbit satellites considered in this study case is aligned with satellite velocity and hence close to the drag vector. Consequently, the along-track component of the stochastic accelerations provides a measurement of residual accelerations due to drag model errors and hence, errors in the nominal density model. With GPS tracking data every 5 minutes and global coverage, this developed approach in this case study generates drag measurements which are more or less equal when compared to data from onboard accelerometers, and better than data from ground radar and optical trackers in terms of precision and resolution. Errors in the measured densities can be decreased by obtaining data from several satellites over a long period of time in the set of parameters related to density (Kuang, 2014).

McLaughlin studied an approach in which POE data are used as observations in a sequential orbit determination scheme that estimates ballistic coefficient and density. In this case study, the Orbit Determination Tool Kit (OTDK, AGI) was used for density estimation along path along the track of the *CHAMP* and *GRACE* satellites. The POE data were input in the sequential processing, filtering and smoothing to derive time-variable ballistic coefficients and densities. The figure below compares the measured, modelled and POE estimated densities from GNSS data of three satellites which are *CHAMP*, *GRACE* and *TerraSAR*-X on 26-27 of September 2007.

Results confirmed that POE based densities are as accurate as densities obtained from onboard accelerometers in terms of large-scale changes, but might not be so in terms of variations for higher frequencies (McLaughlin, 2012).

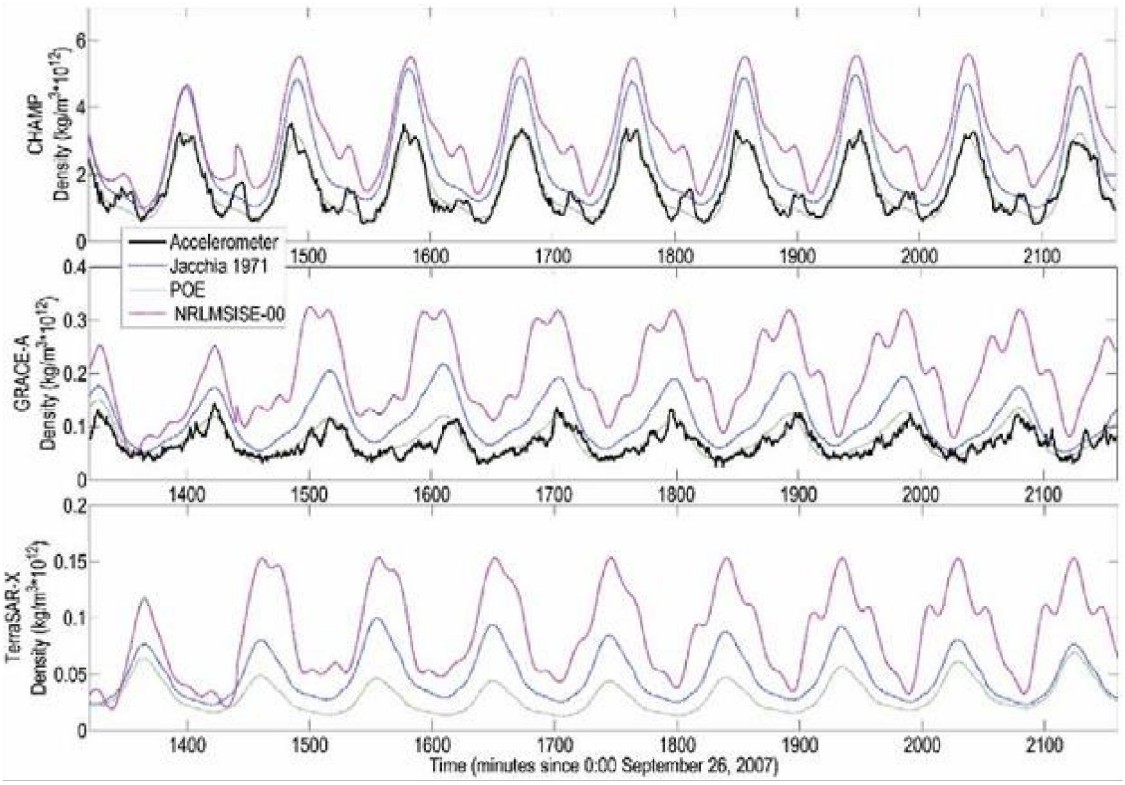

Figure 5.3 Measured, modelled and POE based densities from ***CHAMP***, ***GRACE*** and ***TerraSAR***-X on 26-27 of September 2007 (McLaughlin, 2012).

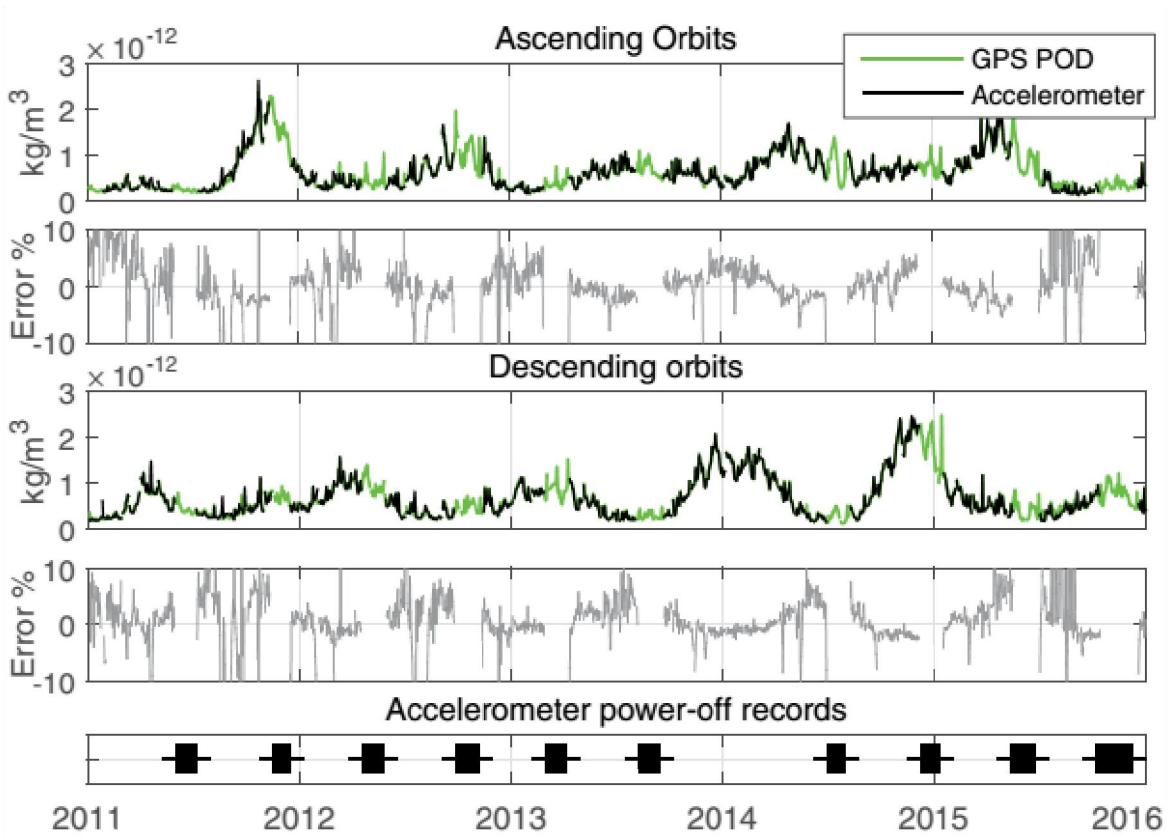

Figure 5.4 Average densities and error differences between POE-based (green colored) and accelerometer-based (black colored) densities separated in ascending and descending orbits. The last line is accelerometer turned off mode (Calabia, 2015).

The use of POD least squares estimators to compute measurements of density is a complex task for obtaining the non-gravitational accelerations derived from differentiation of POE. According to Calabia el at 2015, except for a periodic systematic error of unknown origin, the differentiation requires increase of time that reduce the arc to chord error at given threshold. Then, the authors investigated mass densities inferred through differentiation of POE and results in the figure below show that the highest rate of the differences is up to 10%, and during low-density periods the differences remain at 5% at background densities.

5.3. Density determination using Two-Line Element data.

The final technique to be described consists in deriving data on density of the thermosphere by analyzing sets of two-line elements (TLEs) data of an orbiting satellite which is tracked from the ground and then use these TLEs for density computations. On one hand, this method features quick access to data, long-term coverage database of past years and use on many different orbiting objects; in other hand, it lacks temporal resolution (Doornbos, 2011).

This method is considered for the worst scenario of femtosatellite operation, for instance if accelerometers or/and GNSS receiver failures.

Card #	Satellite Number	Class	International Designator			Yr	Epoch Day of Year (plus fraction)	Mean motion derivative (rev/day /2)	Mean motion second derivative (rev/day2 /6)	Bstar (/ER)	Eph	Elem num	Chk Sum
			Year	Lch#	Piece			S	S.	S. S E			
1	16609	U	86017A			93	352.53502934	.00000788 9	00000-0	10529-3	0		342
	Inclination (deg)					Right Ascension of the Node (deg)		Eccentricity	Arg of Perigee (deg)	Mean Anomaly (deg)	Mean Motion (rev/day)		Epoch Rev	Chk
2	16609		51.6190			13.3340		0005770	102.5680	257.5950	15.59114070		44786	9

Figure 5.5 Two-Line Element set format (Vallado, 2012).

The two-line element (TLE) is a very compact format to show orbital data of space objects including their orbital elements in just two lines. The figure above illustrates a single TLE as an example where each of these lines contains the object identifier and its orbital elements. The first TLE line provides the epoch, the 1st and 2nd derivative of mean motion and other parameters of force model; the second TLE line provides fitted Kepler element data. To recreate the space objects trajectory fitted to the observation data the Simplified General Perturbations 4 (SGP4) propagator with the TLE data has to be applied. The TLE free available database is daily updated, but very early TLE database lacks accuracy and frequency updates.

Picone's approach for density derivation from TLE mean mean-motion data is summarized by Doornbos et al 2011, and is provided in the following section.
The drag acceleration is expressed as

$$r''_D = -\frac{1}{2}\frac{SC_D}{m}\rho V^2 \quad \textbf{(5.6)}$$

from which the ballistic coefficient (B or inverse B') is defined as

$$B' = \frac{1}{B} = \frac{SC_D}{m} \quad \textbf{(5.7)}$$

The drag acceleration vector is along the orbital plane and hence this allows to apply in-plane perturbation equation which can be expressed as

$$\frac{da}{dt} = \frac{2a^2V}{\mu} r'' u_A \quad \textbf{(5.8)}$$

By making use of an along-track unit vector $u_A = V$ and substituting Equations 5.6 and 5.7 into 5.8, we find

$$\frac{da}{dt}|_a = -\frac{a^2}{\mu} B'\rho V^3 \quad \textbf{(5.9)}$$

which describes that the decrease of semi-major axis is due to drag acceleration.

Moreover, according to Doornbos et al 2011, the osculating semi-major axis *a* is distinguished from the mean semi-major axis a_M that is defined by SGP4 from which the noise perturbations due to gravitational field of the Earth are removed. Furthermore, for LEO satellites the density is large, and then perturbations due to solar radiation pressure are neglected in comparison to drag.

Using the mean motion (Equation 5.10), which determines the number of revisits per unit time,

$$n = \sqrt{\frac{\mu}{a^3}} \quad \textbf{(5.10)}$$

then the mean semi-major axis is rewritten using the mean mean-motion n_M which is one of the parameters included in TLE data. Hence

$$\frac{d}{dt} n_M \cong \frac{3}{2}\mu^{-\frac{2}{3}} n_M^{\frac{1}{3}} B'\rho V^3 \quad \textbf{(5.11)}$$

After that, Equation 5.11 is integrated over the period of time between two of TLEs with epochs t_i and t_k which results in

$$n_M(t_k) - n_M(t_i) \approx \frac{3}{2}\mu^{-\frac{2}{3}} \oint_{t_i}^{t_k} n_M^{\frac{1}{3}} B' \rho V^3 \, dt \tag{5.12}$$

Consequently, from Equation 5.12 the observable density is derived as the velocity-weighted average density along the trajectory of satellite's over the period of time between t_i and t_k. Hence, also having $t_{ik} = (t_{ik} + t_k)/2$

$$\rho_O(t_{ik}) \cong \frac{\frac{2}{3}\mu^{\frac{2}{3}}[n_M(t_k) - n_M(t_i)]}{\oint_{t_i}^{t_k} n_M^{\frac{1}{3}} B\prime \rho V^3} = \frac{\oint_{t_i}^{t_k} n_M^{\frac{1}{3}} B\prime \rho V^3 dt}{\oint_{t_i}^{t_k} n_M^{\frac{1}{3}} B\prime \rho V^3 dt} \tag{5.13}$$

Then, the integrals of the ballistic coefficient and mean mean-motion over the time are approximated by constants. The *B'* (estimated or modelled value) remains constant while $n_M(t)$ during the time is approximated by the average of two values at the endpoints

$$n_M(t_{ik}) = \frac{n_M(t_k) + n_M(t_i)}{2} \tag{5.14}$$

Thus, in Equation 5.13 these substitutions result in

$$\rho_O(t_{ik}) \cong \frac{\frac{2}{3}\mu^{\frac{2}{3}}[n_M(t_k) - n_M(t_i)]}{\left(\frac{n_M(t_k) + n_M(t_i)}{2}\right)^{\frac{1}{3}} B\prime \oint_{t_i}^{t_k} V^3 dt} \tag{5.15}$$

This equation can be employed using the two values of n_M which are actually included in the pair of TLEs, in combination with the integrated velocities obtained from using the TLE data with the SGP4 propagator.

Additionally, the velocity-weighted average model density along the trajectory of the satellite is equivalently defined as

$$\rho_M(t_{ik}) = \frac{\oint_{t_i}^{t_k} \rho_M V^3 dt}{\oint_{t_i}^{t_k} V^3 dt} \tag{5.16}$$

In this evaluation of equation, the positions of the satellite (which are obtained from the SGP4 propagator) are one input to the density model, in order to determine the densities $\rho_M(t)$ at each time step required for the numerical computation of the integral (Doornbos, 2011).

While using the described algorithm to process TLE data into observations of the density the user has to deal with several practical considerations such as TLE

selection, appropriate objects in space selection, the choice of time interval and ballistic coefficient values selection.

5.4. Use of the three methods.

To conclude, the use of three methods described for determination of the thermosphere density is completely feasible, and they would be potentially implemented for analysis of the data obtained from the proposed mission.

Even if the accelerometers perform flawlessly, the other two methods will be exploited to check the soundness of local determinations of the density. The extra burden of analyzing these data will be taken over by the ground segment of the mission, and then the femtosatellite will not have further workloads. The gains are much higher than the cited extra work, as it will provide independent self-consistency tests for the whole mission.

Chapter 6

CONCLUSION

6.1. Conclusions

The miniaturization paradigm of space systems provides universities and small companies the opportunity to develop very small satellite missions due to its associated significant reduction in cost. This relatively new approach can be implemented to design mission that focus on a single objective in comparison to traditional large satellites that are designed to meet wide range tasks. Hence, these new small satellites can be used for science and education, communication and remote sensing in its appropriate level of feasibility.

In conclusion, from the development of the proposed mission analysis all our original objectives, established at the beginning of the project, have been achieved:

- Optimal preliminary design of the femtosatellite, with a spherical shape, has been presented and satisfies the requirements established by the science mission goals.
- Commercial-of-the-shelf (COTS) sensors and devices with low mass and power consumption, such as set of three single axis accelerometers and global navigation satellite system (GNSS) receiver based on microelectromechanical systems (MEMS) technology, have been chosen.
- Optimal orbit design and analysis have been discussed, particularly femtosatellites dispersion techniques along orbit planes using ESA's Debris Risk Assessment and Mitigation Analysis (DRAMA) software tool.
- Data gathering strategy and communication architecture have been developed where data rates and link budget were defined. The link budget gives ample margin for data downlink.
- Thermal, power and mass budgets have been selected and examined to meet mission requirements.
- Alternative mission scenarios were identified and evaluated to fulfil mission success (albeit with reduced scope) in case of accelerometers failure or even bus failure. In all cases we avoid complete loss-of-mission scenarios.

It can be stated that we managed to cover almost completely the aspects of the proposed mission for thermospheric density determination, and to achieve all objectives established at the beginning.

6.2. Future work

Regarding to future work, it has to be mentioned that there are some aspects of proposed mission to be studied in-depth. Firstly, the thermal balance during operation can be suggested for reassessment in dynamic conditions close to reality; also, the one node approximation is wat too simplistic.

Secondly, the analysis of all players in the market of rockets and then the choice of the exact launcher among current ones with deployment assistance technique which fit our proposed femtosatellites.

One of the most serious problems is related to satellites' dispersion. We have seen that passive methods based on changing the ballistic coefficients are way too slow. A dispersion mechanism related with the injection system from the launcher could, at least in principle, play an important role in this regard.

Another salient problem is related to the battery. As the electronics are embedded in the aerogel, once the femtosatellite is built it will be impossible to gain access to its payload without damaging the aerogel and the plastic cover. But, if the satellite is active from the moment of its construction, the battery will be depleted when the femtosatellite achieves orbit. We envision two possibilities: a system that activates the dormant satellite when ejected into orbit, or a wireless charging system that fills the battery while the satellites are still in the dispenser. Both possibilities are compatible wit a dead launch.

Finally, the actual manufacture process of femtosatellite and verification tests are specified as the next level of project development.

BIBLIOGRAPHY

[1] Calabia, A., & Jin, S. (2015). GPS-based Non-Gravitational Accelerations and Accelerometer Calibration. *Satellite Positioning - Methods, Models and Applications* (March).

[2] CivilsPro. (2018). *Composition and Structure of Atmosphere*. Retrieved from https://www.civilspro.com/composition-of-atmosphere/

[3] Doornbos, E. (2011). *Thermospheric Density and Wind Determination from Satellite Dynamics.* Ph.D. dissertation, Delft Univ. Technol., Delft, The Netherlands, 2011.

[4] Fernandez, M. (2011). *Mission analysis of QB50 , a nanosatellite intended to study the lower thermosphere Acknowledgments.* MSc thesis, University of Liège, Belgium, 2011.

[5] Fraknoi, A. (2016). *Solar Activity above the Photosphere - Astronomy - OpenStax*. Retrieved from https://openstax.org/books/astronomy/pages/15-3-solar-activity-above-the-photosphere

[6] Heller, T. (2018). *How James Hansen And Michael Mann Destroyed Climate Science | Real Climate Science*. Retrieved from https://realclimatescience.com/2018/05/how-james-hansen-and-michael-mann-destroyed-climate-science/

[7] HighTechMaterialSolutions. . *Silica Aerogel*. Retrieved from https://www.hightechmaterialsolutions.com/silica-aerogel

[8] Ippolito, L. (2008). *Satellite Communications Systems Engineering: Atmospheric Effects, Satellite Link Design and System Performance.*

[9] Janson, S., & Barnhart, D. (2013). The Next Little Thing : Femtosatellites. *27th Annual AIAA/USU Conference on Small Satellites* (310), 1-18.

[10] Jin, S., Calabia, A., & Yuan, L. (2018). Thermospheric Variations from GNSS and Accelerometer Measurements on Small Satellites. *Proceedings of the IEEE, 106*(3), 484-495.

[11] Kuang, D., Desai, S., Sibthorpe, A., & Pi, X. (2014). Measuring atmospheric density using GPS-LEO tracking data. *Advances in Space Research, 53*(2), 243-256.

[12] Larson, W., & Wertz, J. (1999). *Space mission analysis and design / edited by.* Dordrecht [etc.] :: Kluwer Academic,.

[13] Maxim integrated. (2010). Max2769. *Datasheet*, 23.

[14] McLaughlin, C., Lechtenberg, T., Fattig, E., & Krishna, D. (2012). Estimating density using precision satellite orbits from multiple satellites. *Journal of the Astronautical Sciences, 59*(1-2), 85-101.

[15] Microchip Technology, I. (2016). Pic18 F1Xk22. *18*(L) Rretrieved from http://ww1.microchip.com/downloads/en/DeviceDoc/40001365F.pdf

[16] Micron. (2010). M25P64 Serial Flash Memory. *16*(March), 55. Retrieved from https://www.alldatasheet.net/datasheet-pdf/pdf/99716/STMICROELECTRONICS/M25P64.html

[17] Pisacane, V. (2005). *Fundamentals of space systems / edited by.* Oxford :: Oxford University Press,.

[18] Report. (2014). *DRAMA Final Report Upgrade of ESA's Space Debris Mitigation Analysis Tool Suite.*

[19] Silicon Designs, I. (2015). Available G-Ranges Low Cost Sdi 2210 , 2260 & 2266 High Performance Sdi 2220 & 2276 Performance By G Range Performance. (Dc), 1-5. Retrieved from https://www.silicondesigns.com/data-sheets

[20] SiliconLabs. (2014). Si4x55-C. 1-39. Retrieved from https://www.silabs.com/documents/public/data-sheets/Si4x55-C.pdf

[21] Sutton, E., Nerem, R., & Forbes, J. (2007). Density and winds in the thermosphere deduced from accelerometer data. *Journal of Spacecraft and Rockets, 44*(6), 1210-1219.

[22] Svalbardblues.com. (2020). *Kongsberg Satellite Services | SvalSat | Longyearbyen | SVALBARD*. Retrieved from https://www.svalbardblues.com/svalbard/bedrifter/kongsberg-satellite-services/

[23] Tadiran. (2012). MODEL TL-5930. *Current*, 2-3. Retrieved from http://www.tadiranbat.com/assets/tl-5920.pdf

[24] Vallado, D., & Cefola, P. (2012). Two-line element sets - Practice and use. *Proceedings of the International Astronautical Congress, IAC, 7* (January 2012), 5812-5825.

[25] Wakker, K. (2015). *Fundamentals of Astrodynamics.*

[26] Wekerle, T., Filho, J., da Costa, L., & Trabasso, L. (2017). Status and trends of smallsats and their launch vehicles - An up-to-date review. *Journal of Aerospace Technology and Management, 9*(3), 269-286.

[27] Zhao, Z., Wang, Z., & Zhang, Y. (2019). A spherical micro satellite design and detection method for upper atmospheric density estimation. *International Journal of Aerospace Engineering, 2019*.

ANNEX A.

1 - Accelerometer parameters

(obtained from https://www.silicondesigns.com/data-sheets).

PERFORMANCE BY G RANGE

INPUT RANGE	SENSITIVITY, DIFFERENTIAL	*FREQUENCY RESPONSE (TYPICAL, 5%)	*FREQUENCY RESPONSE (TYPICAL, 3 DB)	*FREQUENCY RESPONSE (MINIMUM, 3 DB)	OUTPUT NOISE, DIFFERENTIAL (RMS, TYPICAL)	MAX. MECHANICAL SHOCK (0.1 MS)
g	mV/g	Hz	Hz	Hz	µg/(root Hz)	g (peak)
±2	2000	0 – 250	0 – 525	0 – 300	10	2000
±5	800	0 – 400	0 – 800	0 – 420	15	
±10	400	0 – 700	0 – 1100	0 – 660	23	5000
±25	160	0 – 1300	0 – 1750	0 – 1050	38	
±50	80	0 – 1600	0 – 2100	0 – 1400	60	
±100	40	0 – 1700	0 – 3000	0 – 1700	121	
±200	20	0 – 1900	0 – 3600	0 – 2100	243	
±400	10	0 – 2000	0 – 4200	0 – 2400	475	

By Model: $V_{DD}=V_R=5.0$ VDC, $T_C=25$ °C *Single ended sensitivity is half of values shown.*

PARAMETER	MIN	TYP	MAX	UNITS
Bias Calibration Error (%)		0.25	0.6	± % of span
Bias Calibration Error (mV)		25	60	± mV
Scale Factor Calibration Error [1]		0.5	1.25	± %
Non-Linearity (-90 to +90% of span) [1]		0.15	0.5	± % of span
Cross Axis Sensitivity		2	3	± %
Power Supply Rejection Ratio	50	>65		dB
Output Impedance		1		Ω
Output Common Mode Voltage		2.5		VDC
Operating Voltage	8		32	VDC
Operating Current (AOP & AON open)		7	10.5	mA DC
Operating Temperature	-55		+125	°C
Mass 2210-2220 / 2260 / 2266-2276 (not including cable)		10 / 6 / 9		grams
Cable Mass (3' integrated cable, 2210, 2220, 2260)		14		grams/meter

2 - Microchip PIC18F1XK22
(obtained from http://ww1.microchip.com/downloads/en/DeviceDoc/40001365F.pdf).

PIC18(L)F1XK22

TABLE 1-1: DEVICE FEATURES FOR THE PIC18(L)F1XK22 (20-PIN DEVICES)

Features	PIC18F13K22	PIC18LF13K22	PIC18F14K22	PIC18LF14K22
Voltage Range (1.8 - 5.5V)	2.3-5.5V	1.8V-3.6V	2.3-5.5V	1.8V-3.6V
Program Memory (Bytes)	8K		16K	
Program Memory (Instructions)	4096		8192	
Data Memory (Bytes)	256		512	
Operating Frequency	DC – 64 MHz			
Interrupt Sources	30			
I/O Ports	Ports A, B, C			
Timers	4			
Enhanced Capture/ Compare/PWM Modules	1			
Serial Communications	MSSP, Enhanced USART			
10-Bit Analog-to-Digital Module	12 Input Channels			
Resets (and Delays)	POR, BOR, RESET Instruction, Stack Full, Stack Underflow, $\overline{\text{MCLR}}$, WDT (PWRT, OST)			
Instruction Set	75 Instructions, 83 with Extended Instruction Set Enabled			
Packages	20-Pin PDIP, SSOP, SOIC QFN (4x4x0.9mm)			

3 - Micron's VDFPN8 Flash memory module
(obtained from https://www.alldatasheet.net/datasheet-pdf/pdf/99716/STMICROELECTRONICS/M25P64.html).

Logic diagram (left) and VDFPN connection (right).

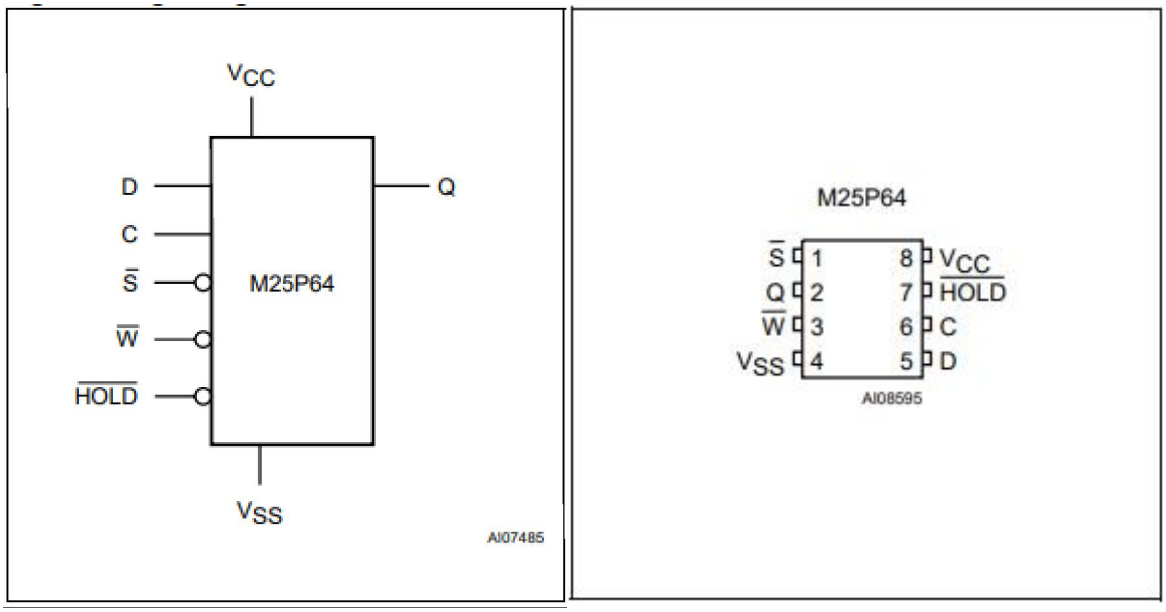

Bus Master and Memory devices on the SPI Bus.

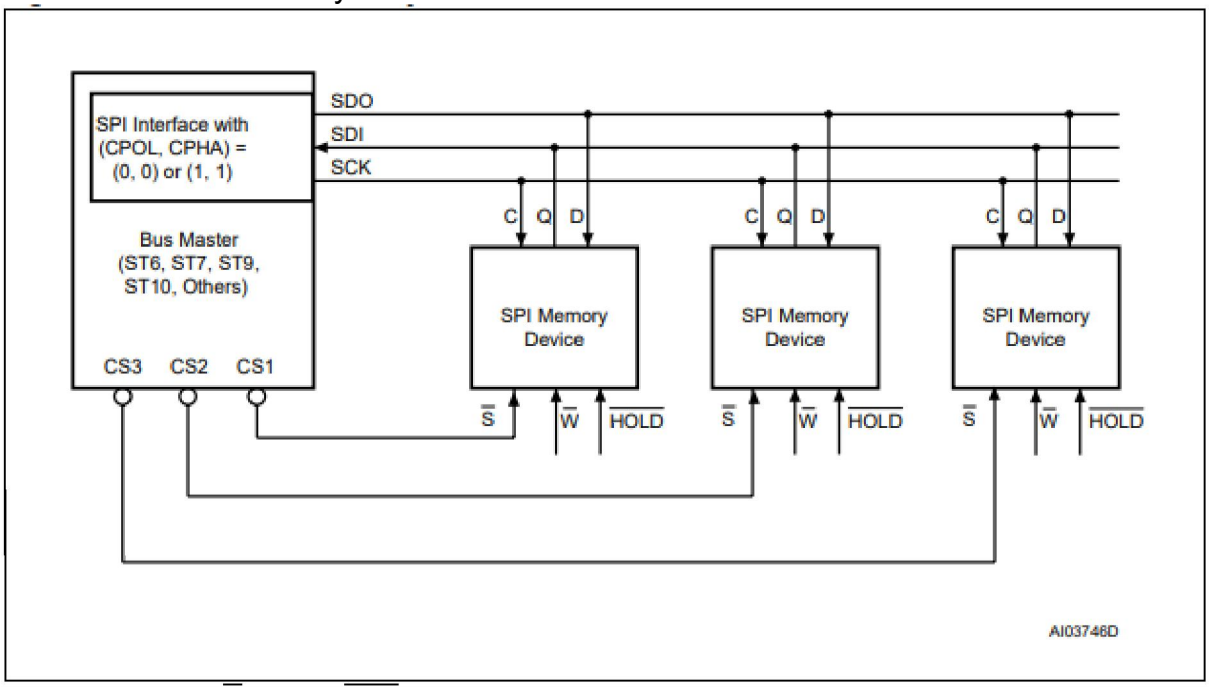

4 - Si4455 transmitter

(obtained from https://www.silabs.com/documents/public/data-sheets/Si4x55-C.pdf).

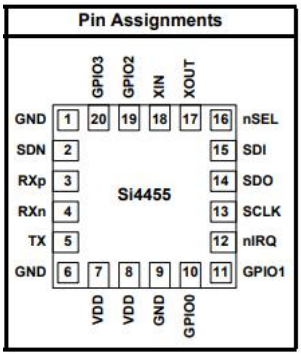

Functional Block Diagram

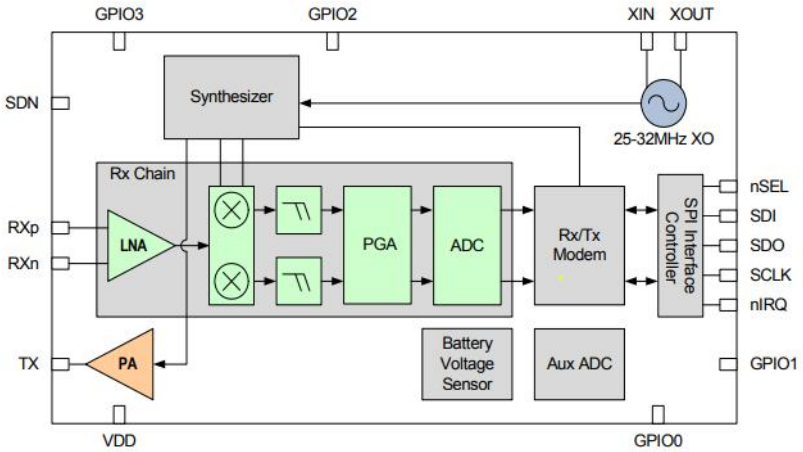

Table 1. DC Characteristics

Parameter	Symbol	Test Condition	Min	Typ	Max	Unit
Supply Voltage Range	V_{DD}		1.8	3.3	3.6	V
Power Saving Modes	$I_{Shutdown}$	RC oscillator, main digital regulator, and low power digital regulator OFF.	—	30	—	nA
	$I_{Standby}$	Register values maintained.	—	40	—	nA
	I_{Ready}	Crystal Oscillator and Main Digital Regulator ON, all other blocks OFF.	—	1.8	—	mA
	$I_{SPI\ Active}$	SPI active state		1.5		mA
TUNE Mode Current	I_{Tune_RX}	RX Tune	—	6.8	—	mA
	I_{Tune_TX}	TX Tune	—	7.1	—	mA
RX Mode Current	I_{RX}	Measured at 40 kbps, 20 kHz deviation, 315 MHz	—	10.9	—	mA
TX Mode Current	I_{TX}	+10 dBm output power Measured on direct tie RF evaluation board at 868 MHz	—	19	—	mA
		+13 dBm output power Measured on direct tie RF evaluation board at 868 MHz	—	24	—	mA

Note: All minimum and maximum values are guaranteed across the recommended operating conditions of supply voltage and from –40 to +85 °C unless otherwise stated. All typical values apply at VDD = 3.3 V and 25 °C unless otherwise stated.

5 - Primary battery TL 5920 iXtra

(obtained from http://www.tadiranbat.com/assets/tl-5920.pdf).

TECHNICAL DATA

(Typical values @+ 25ºC for batteries stored for one year or less)

Nominal capacity @ 3 mA, to 2 V	8.5 Ah
Rated voltage	3.6 V
Maximum recommended continuous current	230 mA
Maximum pulse current capability	400 mA
Weight	49.5 g (1.75 oz)
Volume	26 cc
Operating temperature range	-55 ºC to +85 ºC
Li metal content	approx. 2.5 g
U.L. Component Recognition, MH 12193